Solid State Sciences 183 (2027) 108540

Contents lists available at ScienceDirect

Solid State Sciences

journal homepage: www.elsevier.com/locate/ssscie

Nonlinear defect interactions and performance limitations in Sb_2Se_3 solar cells: a factorial SCAPS-1D sensitivity analysis

J.M. Delgado-Sanchez [a,*], E. Artegiani [b], B. Rezek [c], A. Romeo [b]

[a] Department Applied Physics I, Escuela Técnica Superior de Agronomía, University of Seville, Ctra. Utrera km 1, Seville, 41013, Spain
[b] LAPS-Laboratory for Photovoltaics and Solid-State Physics, Department of Computer Science, University of Verona, Ca' Vignal 1, Strada Le Grazie 15, Verona, 37134, Italy
[c] Faculty of Electrical Engineering, Czech Technical University, Technická 2, Prague 6, Czech Republic

ARTICLE INFO

Keywords:
Sb_2Se_3 solar cells
SCAPS-1D
Band tail states
Double donor defects
Defect hierarchy

ABSTRACT

Despite considerable efforts, efficiencies of Sb_2Se_3 solar cells remain on a plateau limited by voltage deficits and carrier collection losses. Here, a SCAPS-1D model calibrated to the current record-efficiency Sb_2Se_3 solar cell is used for full-factorial sensitivity analysis to understand and quantify the joint impact of representative donor, acceptor, double donor-like, and band tail defects, complemented by a selective-reduction analysis of the CdS/Sb_2Se_3 interface defects. The simulations reveal, for the calibrated parameter set, a co-limited regime governed by a statistically significant, non-additive interaction between double donor-like and band tail defects. Band tail states, commonly associated with structural disorder, emerge as the dominant bulk voltage-limiting defect by reducing quasi-Fermi level splitting and enhancing distributed non-radiative recombination, degrading the device gradually without a critical threshold. Double donor-like defects control carrier extraction through compensation of the native p-type absorber: when their ionized charge exceeds the acceptor density, the junction field reverses at $\sim 10^{15}$ cm^{-3} and carrier collection collapses, a threshold that shifts by more than an order of magnitude in the presence of band tail states. Near open circuit, recombination at the CdS/Sb_2Se_3 interface dominates, and its passivation offers the largest single efficiency gain. We show that the defect interactions create a two-dimensional performance landscape in Sb_2Se_3, where band tail recombination and donor compensation act through different physical pathways and jointly limit the efficiency of the calibrated device. The resulting two-dimensional defect-tolerance map provides quantitative practical guidelines for defect engineering and further efficiency improvements of Sb_2Se_3 solar cells.

1. Introduction

Antimony selenide (Sb_2Se_3) has emerged as a promising absorber material for thin-film solar cells [1–3]. It features an absorption coefficient exceeding 10^5 cm^{-1} [4,5] and nearly ideal direct bandgap (1.1-1.2 eV) [5]. Sb_2Se_3 binary chemistry relies on earth-abundant and low-toxicity elements. The quasi-one-dimensional (Q1D) structure consists of $[Sb_4Se_6]_n$ ribbons linked by van der Waals forces [1]. Over the past decade, significant progress has been achieved in Sb_2Se_3 device performance, with reported power conversion efficiencies rising from 2.25 % in 2014 [6], to 4.7 % in 2015 [7], 7.04 % in 2018 [8], to the current record of 10.57 % achieved in 2022 [9]. Nevertheless, the efficiencies achieved remain substantially below the theoretical potential of the material.

A major factor limiting device performance is the presence of electronic defects that influence carrier recombination, electrostatics, and charge transport. Historically, the ribbon configuration of Sb_2Se_3 was thought to ensure grain boundaries free of dangling bonds [10]. However, experimental open-circuit voltage (V_{oc}) limitations challenge this benign boundary concept [11,12]. Prior theoretical calculations and experimental studies have identified several intrinsic point defects that can form in Sb_2Se_3 including vacancies, antisites, and defect complexes. Depending on their charge state and formation conditions, these defects may behave as donor or acceptor like states and thus modify the effective doping level of the absorber [13]. Such defects can introduce deep electronic levels within the band gap that act as recombination centers, reducing carrier lifetime and limiting the achievable V_{oc}. Beyond isolated

This article is part of a special issue entitled: defect-controlled published in Solid State Sciences.

* Corresponding author.
E-mail address: jdelgado17@us.es (J.M. Delgado-Sanchez).

https://doi.org/10.1016/j.solidstatesciences.2026.108540
Received 7 July 2026; Received in revised form 13 October 2026; Accepted 27 October 2026
Available online 28 October 2026
1293-2558/© 2026 The Authors. Published by Elsevier Masson SAS. This is an open access article under the CC BY-NC license (http://creativecommons.org/licenses/by-nc/4.0/).

point defects, structural disorder can also introduce band tail states extending from the band edges into the band gap. These states are commonly associated with grain boundaries, structural disorder, or extended defect complexes in the material.

Recent progress in the identification and characterization of defects in Sb_2Se_3 has been driven by both theoretical modeling and experimental techniques, such as admittance spectroscopy (AS) and Deep-Level Transient Spectroscopy (DLTS). Stoliaroff [14] and Dong [15] have proposed, using DFT calculations, a general taxonomy of intrinsic point defects in Sb_2Se_3, classifying them into donor- and acceptor-type configurations according to their chemical origin and energetic position within the bandgap. In parallel, Huang [16] provided a description of the intrinsic defect chemistry, emphasizing the dominant role of antisite defects and the delicate balance between native vacancies and antisite configurations in establishing the intrinsic p-type character of Sb_2Se_3. Although these works differ in how explicitly they attribute conductivity to specific isolated defects versus compensation equilibria, they converge on the central role of Sb_2Se_3 defect chemistry in governing electronic properties. There is a general agreement that single acceptor defects, primarily antimony vacancies (V_{Sb}) and selenium-on-antimony antisites (Se_{Sb}), are the main contributors to p-type conductivity. These defects introduce relatively shallow acceptor levels located ~0.1-0.2 eV above the valence band minimum, enabling efficient hole generation and defining the intrinsic doping behavior of the material.

In contrast, donor-type defects exhibit a higher degree of ambiguity across literature [14–16]. Single donors, such as selenium vacancies (V_{Se}), are widely recognized as compensating centers that reduce free hole concentration and contribute to V_{oc} losses. Antimony-on-selenium antisites (Sb_{Se}) also act as compensating donors but can adopt multiple charge states and are therefore frequently associated with double donor behavior. However, the nature of so-called double donor configurations remains less consistently defined. While earlier interpretations (e.g., Stoliaroff [14]) treat them as distinct deeper donor states associated with complex defect configurations or multiple charge transition levels, more recent work by Dong [15] suggests that these apparent double donor signatures may instead emerge from defect coupling effects and local structural relaxation in the quasi-one-dimensional lattice, rather than representing an independent fundamental defect class. This interpretation is further reinforced by Wijesinghe, Longo and Hutter [17], who argue that in quasi-one-dimensional materials such as Sb_2Se_3, the concept of isolated point defects is often insufficient, and that double donor-like behavior should be understood as the emergent electronic response of interacting defect ensembles and structural disorder.

Beyond discrete point defects, the electronic landscape of Sb_2Se_3 is also strongly influenced by continuous disorder-induced states [18]. The valence band tail arises from energy fluctuations in Se orbitals associated with structural disorder, whereas the conduction band tail originates from disorder in Sb orbitals. These localized band-edge fluctuations contribute to the formation of an extended Urbach tail, effectively broadening the band edges and introducing a continuum of shallow localized states [19,20]. As crystalline quality deteriorates, the density and energetic width of these tail states increase, and it has been proposed that the resulting carrier localization and screening of ionized charges reduce the effective built-in electric field and degrade charge separation.

This defect landscape is further complicated by the presence of deep-level traps experimentally observed in Sb_2Se_3 solar cells. Hobson [13] and Dong [15] identified several critical defects (E_1, E_2 and E_3) using DLTS and admittance spectroscopy, with activation energies between 0.35 and 0.69 eV relative to the band edges. These states act as efficient non-radiative recombination centers, strongly limiting carrier lifetime. In parallel, the current efficiency record of 10.57 % for Sb_2Se_3 solar cells was reported by Zhao [9], who identified two dominant hole traps ($H_1 = 0.43$ eV and $H_2 = 0.47$ eV) via admittance spectroscopy. These traps were chemically linked to deep-level configurations of Se_{Sb} antisites (Se_{Sb1} and Se_{Sb2}) located at inequivalent lattice sites. Since Se_{Sb} antisites have also been associated with shallow acceptor levels [14–16], these assignments suggest that the same antisite can give rise to either shallow or deep states, depending on its lattice site and on the charge-state transition involved. In contrast to shallow acceptors, these deep states act as recombination centers rather than dopants, and their suppression was critical to achieving record device performance.

Although the electronic structure and formation energetics of many defects in Sb_2Se_3 have been extensively studied, the impact of their interplay on device level operation remains insufficiently understood and quantified [3,8,21–23]. In particular, while microscopic analyses provide detailed insight into defect origin and energetics, they do not systematically resolve how different defect populations govern internal electrostatics, carrier transport regimes, and macroscopic photovoltaic parameters. This disconnection prevents the establishment of clear defect-tolerance limits and obscures identification of the most performance-limiting defect configurations.

Unlike most SCAPS-1D studies, which use the simulator as a device-optimization tool to tune layer thicknesses, doping or band alignments, the present work uses it to analyze defect physics and multivariable defect sensitivity, treating the defect populations as the central object of study rather than as auxiliary model parameters. To this end, comprehensive solar cell-level simulations of defect-induced performance degradation in Sb_2Se_3 solar cells are performed. A numerical model based on SCAPS-1D was first developed and calibrated to reproduce the experimental J-V and EQE response of the record-efficiency solar cell [9]. Subsequently, a systematic sensitivity analysis is performed to quantify the impact of different defect populations, including single donor, single acceptor, double donor and band tail states, together with interface defects, on charge transport and recombination dynamics. This approach enables the extraction of defect density thresholds, defined by an objective criterion, and the shape of the transition for each defect class, and their influence on internal electric field distribution, SRH recombination activity, carrier transport regime, quasi-Fermi level splitting, and current-voltage characteristics. In particular, the analysis distinguishes between defects that degrade the device through electrostatic compensation, reversing the junction field and driving carriers towards interface recombination, and defects that act through distributed bulk recombination. The interaction between the two dominant defect classes is quantified through factorial and response-surface analysis.

This simulation framework thereby establishes a quantitative link between microscopic defect physics and macroscopic device performance, provides a defect-tolerance map that clarifies the relative role and interplay of different defect species in limiting the efficiency of the calibrated Sb_2Se_3 solar cell, and offers practical design guidelines for material and process optimization.

2. Methodology

2.1. SCAPS software and theoretical foundations

Numerical simulations were performed by SCAPS-1D, a one-dimensional solar cell simulation software developed at the University of Ghent [24]. SCAPS-1D is widely used in the photovoltaic community for the theoretical analysis of thin-film solar cells, particularly for chalcogenide-based devices such as CIGS, CZTS and Sb_2Se_3 [25–27]. Detailed description of SCAPS modeling and the algorithms can be found in Refs. [24,28,29].

Briefly, SCAPS-1D mathematical framework consists of the Poisson equation (Eq. (1)), which relates the electrostatic potential (ϕ) to the space charge distribution, together with the continuity equations for both electron (Eq. (2)) and holes (Eq. (3)). It also incorporates the drift-diffusion current equations for electrons (Eq. (4)) and holes (Eq. (5)), expressed in terms of the quasi-Fermi level gradients.

$$\frac{d}{dx}\left(-\varepsilon(x)\frac{d\phi}{dx}\right) = q\left[p(x) - n(x) + N_D(x) - N_A(x) + \rho_{trap}(x)\right] \quad (1)$$

$$-\left(\frac{1}{q}\right)\frac{\partial J_n}{\partial x} - R_n + G = \frac{\partial n(x)}{\partial t} \quad (2)$$

$$-\left(\frac{1}{q}\right)\frac{\partial J_p}{\partial x} - R_p + G = \frac{\partial p(x)}{\partial t} \quad (3)$$

$$J_n = n(x)\,\mu_n\,\frac{\partial E_{Fn}}{\partial x} \quad (4)$$

$$J_p = p(x)\,\mu_p\,\frac{\partial E_{Fp}}{\partial x} \quad (5)$$

where ε is the permittivity, q is the elementary charge, n and p are the free carrier concentrations, N_A and N_D denote the acceptor and donor densities, while ρ_{trap} represents the charge associated with defect traps. J_n and J_p are the electron and hole current densities. R_n and R_p are electron and hole recombination rates, respectively, while G is the carrier generation rate. E_{Fn} and E_{Fp} correspond to the electron and hole quasi-Fermi levels, while μ_n and μ_p are the carrier mobilities.

SCAPS-1D solves these fundamental semiconductor equations under steady-state conditions, using the coupled system of differential equations (ϕ, n, p) or equivalently (ϕ, E_{Fn}, E_{Fp}), considering appropriate boundary conditions at interfaces and contacts. Solar cell performance parameters were evaluated under Standard Test Conditions (STC) using the AM1.5G solar spectrum 1000 W m^{-2} at a temperature of 300 K.

2.2. Device configuration and material parameters

The Sb_2Se_3 solar cell architecture simulated in this work consisted of a glass/FTO/CdS/Sb_2Se_3/Au heterojunction stack. This configuration was inspired by the world-record-efficiency device reported by Zhao [9]. The layer thicknesses, as well as series and shunt resistances, were adopted from this reference to ensure consistency with experimental benchmarks. In this configuration, FTO serves as the transparent conductive oxide (TCO) and CdS acts as the n-type buffer layer, while Sb_2Se_3 functions as the p-type light-harvesting absorber.

Accurate device simulation in SCAPS-1D (version 3.3.11) requires specifying the key physical parameters for each layer. The fundamental material properties used in this study are summarized in Table 1 [25,27, 30–35]. These parameters include the bandgap (E_g), electron affinity (χ), relative permittivity (ε_r), and the effective density of states (N_c, N_v). Carrier mobilities (μ_n, μ_p) and doping concentrations (N_D, N_A) were also defined according to reference literature. Thermal velocities for electrons and holes were set to 10^7 cm/s. The rear interface was modeled using a metal back contact with an appropriate work function (Φ_m) to represent a quasi-ohmic metal/absorber junction. The model was at first calibrated to reproduce the J-V and EQE characteristics reported by Zhao [9]. The agreement between experimental and simulated responses was quantified using MAE, RMSE, NMAE and NRMSE, in addition to the main photovoltaic parameters, and the identifiability of the calibrated parameter set is analyzed in the Supporting Information. Once agreement with the reference device performance was achieved, the calibrated structure was used as the starting point for systematic multi-factorial parametric analysis of bulk and interface properties.

Table 1
Simulation parameters for Sb_2Se_3 and CdS films.

Parameters	Sb_2Se_3	CdS	
Thickness (nm)	1000	60	[9]
Bandgap (eV)	1.1	2.4	[9]
Electron affinity (eV)	4.1	4.2	[30–35]
Relative dielectric permittivity	14.5	10	[30–35]
CB effective density of states (cm^{-3})	2×10^{18}	2.2×10^{18}	[30–35]
VB effective density of states (cm^{-3})	1×10^{19}	1.8×10^{19}	[30–35]
Electron thermal velocity (cm s^{-1})	1×10^{7}	1×10^{7}	[30–35]
Hole thermal velocity (cm s^{-1})	1×10^{7}	1×10^{7}	[30–35]
Electron mobility (cm^2 V^{-1} s^{-1})	16.7	50	[30–35]
Hole mobility (cm^2 V^{-1} s^{-1})	16.7	5	[30–35]
Donor doping N_D (cm^{-3})	-	1×10^{18}	[30–35]
Acceptor doping N_A (cm^{-3})	1×10^{15}	-	[9]
Radiative recombination coefficient (cm^3 s^{-1})	2.2×10^{-9}	-	[30–35]

In accordance with SCAPS-1D practice, the FTO and Au electrodes were not modeled as layers but defined as electrical contacts, i.e. as boundary conditions applied to the CdS and Sb_2Se_3 layers, respectively. The front contact was characterized by a work function of 4.1 eV and surface recombination velocities of 10^8 cm s^{-1} for both electrons and holes. The rear contact was characterized by a work function of 5.4 eV and surface recombination velocities of 10^7 cm s^{-1} for both carriers [34, 35]. Tunnelling was disabled at both contacts. The optical properties of the contacts were taken from a default file of the SCAPS library. Series and shunt resistances of 6.5 Ω cm^2 and 6×10^2 Ω cm^2, respectively, were included in all simulations. The numerical settings used in all simulations are listed in Supporting Information (Table S1). The device was defined in SCAPS as Au/Sb_2Se_3/CdS/FTO, with illumination incident from the FTO side. The absorption coefficients of CdS and Sb_2Se_3 were taken from Refs. [36–38], and were kept constant in all simulations, so that variations in band tail density do not modify the optical absorption.

Single defect sweeps were performed to quantify the density at which each bulk defect becomes performance-limiting. In each sweep the defect of interest was the only bulk defect, while the CdS/Sb_2Se_3 interface defect was kept at its calibrated value (Table 3). N_t in double donor was varied from 10^{14} to 10^{17} cm^{-3}, in 17 logarithmically spaced steps, and N_t in band tail states over 12 densities between 10^{13} and 10^{17} cm^{-3}. The double donor sweep was repeated with band tail states at their calibrated density (10^{16} cm^{-3}) to assess the effect of their interaction on the threshold. Internal profiles were computed for each defect at 12 densities between 10^{13} and 10^{17} cm^{-3}, at V = 0 for the electric field and SRH recombination and at V = V_{oc} for the quasi-Fermi level splitting. Thresholds were defined relative to the device without bulk defects as the density at which J_{sc} decreases by 10 % or efficiency by one absolute percentage point. For the double donor sweep with band tail state states, the band tail-only case was taken as reference. Threshold densities were obtained by linear interpolation in log N_t between adjacent simulation points, and the width of each transition was quantified as the interval in log N_t between $\eta = 0.9\eta_0$ and $\eta = 0.5\eta_0$.

All simulations were performed with a maximum ratio of 1.2 between neighboring mesh points (Table S1). Mesh convergence was verified by repeating the calculations with ratios of 1.6 and 1.1 for the reference device and for a device in the double donor transition region (double donor as the only bulk defect, $N_{DD} = 2 \times 10^{15}\ cm^{-3}$), where J_{sc} is most sensitive to the internal field. In both cases the variation between the coarsest and finest mesh was below 0.25 % in J_{sc} and efficiency, and below 0.02 % in V_{oc} and FF, and the bulk and interface recombination currents were unchanged (Table S2). The corresponding uncertainty in the double donor threshold density is below 1 %. The contour maps were interpolated in OriginPro using spline interpolation from the 13×13 matrix of simulations, all of which converged.

2.3. Defects and recombination mechanisms

Non-radiative recombination in the Sb_2Se_3 absorber layer is modeled using the Shockley-Read-Hall (SRH) formalism. SRH recombination constitutes one of the dominant performance-loss mechanisms in Sb_2Se_3 solar cells due to the high density of defect-induced localized states within the bandgap [39]. These states originate from intrinsic point defects, defect complexes, antisite configurations, and disorder-induced band tail states, which act as carrier trapping and recombination centers. The net recombination rate (R_{SRH}) associated with a given defect level is defined as [40]:

$$R_{SRH} = \frac{np - n_i^2}{\tau_p\,(n + n_1) + \tau_n\,(p + p_1)} \tag{6}$$

where n and p are the free carrier concentrations, and n_i is the intrinsic carrier density. The parameters n_1 and p_1 correspond to the carrier densities when the Fermi level coincides with the defect energy level (E_t). The carrier lifetimes $(\tau_{n,p})$ are determined by the capture cross-sections $(\sigma_{n,p})$ and the total defect density (N_t):

$$\tau_{n,p} = \frac{1}{\sigma_{n,p}\,\nu_{th}\,N_t} \tag{7}$$

where ν_{th} is the thermal velocity of the carrier. Carrier transport and collection are further limited by the diffusion length $(L_{n,p})$, which depends on the diffusion coefficient $(D_{n,p})$, carrier lifetime $(\tau_{n,p})$, thermal voltage (V_T) and carrier mobility $(\mu_{n,p})$, as shown in Eq. (8) and Eq. (9):

$$L_{n,p} = \sqrt{D_{n,p}\,\tau_{n,p}} \tag{8}$$

$$D_{n,p} = V_T\,\mu_{n,p} \tag{9}$$

Beyond discrete point defects, the quasi-1D ribbon structure of Sb_2Se_3 is susceptible to structural disorder and grain boundary fluctuations [8,41]. These imperfections are commonly associated with a distribution of electronic states extending from the band edges into the gap, known as band tails. In the literature, band tails have been linked to a reduction in carrier mobility, an effective narrowing of the optical bandgap, and a major contribution to the V_{oc} deficit observed in experimental solar cells [42–44]. In the present simulations, band tails are represented as exponential distributions of localized electronic states that act as carrier trapping and recombination centers. Carrier mobilities and the bandgap are fixed input parameters (Table 1), so effects on transport, such as mobility reduction, and on the effective bandgap are not included in the model and are mentioned only as physical context.

The electrostatic behavior of the heterojunction is described by the Poisson equation (Eq. (1)), which relates the electrostatic potential to the space charge density. The built-in electric field generated at the CdS/Sb_2Se_3 interface is essential for efficient carrier separation. However, ionized defects contribute to the space charge (ρ_{trap} in Eq. (1)) and can therefore modify the internal field [45]. Depending on the sign and density of their charge, they can weaken the junction field and reduce the depletion width, shifting carrier collection from drift-dominated to diffusion-limited transport, or even reverse it. The electrostatic effect of each defect type is analyzed in Section 3.

To reproduce the experimentally observed electronic landscape of Sb_2Se_3, the SCAPS model incorporates both discrete defect states and disorder-induced band tail distributions. Specifically, three representative point-defect levels and exponential band tails are included to capture the combined effects of compensation, deep recombination, and structural disorder within the absorber. While the general nature of these defect types in Sb_2Se_3 is well established in the literature, the following summarizes their physical interpretation and the specific modeling assumptions adopted in this work:

a) Single donor (V_{Se}): selenium vacancy states act primarily as compensating centers, reducing the effective hole concentration and weakening the built-in electric field. They are modeled here as deep donor-like states (Table 2) consistent with selenium-deficient growth conditions, where their primary role is electrostatic compensation rather than deep recombination.

b) Double donor-like deep states (Sb_{Se}): these states represent deep donor-type recombination centers commonly associated with antimony-on-selenium antisites or defect-coupled configurations. Rather than treating them as strictly isolated point defects, they are modeled here as effective deep electronic states that capture the collective recombination and electrostatic activity of a family of structurally related defect configurations. The double donor defect is assigned to Sb_{Se} antisite configurations as an effective interpretation, consistent with recent interpretations in the literature. This distinction is relevant because the double donor is a multivalent defect whose recombination activity involves multiple charge-state transitions and is therefore represented by two transition levels within the SRH framework, rather than by a single defect level. The double donor is implemented in SCAPS as a single multivalent defect with three charge states (DD^0, DD^+, and DD^{2+}) and two associated transition levels: DD^+/DD^0 at 0.20 eV and DD^{2+}/DD^+ at 0.55 eV below Ec (0.90 and 0.55 eV above Ev; Table 2), with electron and hole capture cross sections of 10^{-15} cm^2 for both transitions. The occupation of the three charge states determines both the SRH recombination rate and the defect charge entering the Poisson equation (Eq. (1)).

c) Single acceptor (V_{Sb}): antimony vacancy states constitute the dominant source of intrinsic p-type conductivity in Sb_2Se_3 and are modeled as shallow acceptor-like levels. Their primary role in the model is to define the equilibrium carrier density rather than to act as efficient recombination centers, given their energetic proximity to the valence band.

d) Valence and conduction band tail states (structural): were modeled in SCAPS-1D as exponential distributions of acceptor-like (valence tail) and donor-like (conduction tail) states, intended to represent the broadening of the density of states caused by structural disorder. In this work, structural disorder is defined operationally through Urbach energy (E_U) and the integrated tail density, and no specific atomic configuration is assumed. The valence-band tail is represented by:

$$N_V(E) = N_{0,V}\,\exp[-(E - E_V)/E_U] \quad (E > E_V) \tag{10}$$

where E is measured from the valence band edge (E_V), $N_{0,V}$ is the density of states per unit energy at the band edge, and E_U is Urbach energy. The total integrated density of each tail is:

Table 3
Sb_2Se_3/CdS interface defect parameters.

Defect type	Sb_2Se_3/CdS
Capture cross section electrons (cm^2)	1.0×10^{-15}
Capture cross section holes (cm^2)	1.0×10^{-15}
Energetic distribution	Single
Energy level with respect to Valence Band edge (eV)	0.60
Total defect density (N_t)	1.0×10^{12} cm^{-2}

Table 2
Bulk defect and band tail parameters for Sb_2Se_3. For the double donor defect, the same electron and hole capture cross sections were used for both transition levels.

Defect type	Single donor (0 / +)	Double donor (0 / + /2 +)	Single acceptor (− /0)	Band Tail (− /0)	Band Tail (0 / +)
Capture cross section electrons (cm^2)	3.3×10^{-15}	1.0×10^{-15}	1.0×10^{-15}	1.0×10^{-17}	1.0×10^{-17}
Capture cross section holes (cm^2)	1.0×10^{-15}	1.0×10^{-15}	1.0×10^{-15}	1.0×10^{-17}	1.0×10^{-17}
Energetic distribution	Single	Single	Single	VB Tail	CB Tail
Energy level with respect to VB edge (eV)	0.40	0.90/0.55	0.25	0.00	0.00
Urbach energy (eV)	-	-	-	0.032	0.032
Total defect density (N_t) (cm^{-3})	4.0×10^{12}	1.0×10^{16}	1.0×10^{14}	1.0×10^{16}	1.0×10^{16}

$$N_t = \int N_V(E)\, dE \tag{11}$$

which is the parameter entered in SCAPS, corresponding to $N_t = 1\times 10^{16}\ cm^{-3}$ (Table 2) in this model. $N_{0,V}$ is derived internally. The conduction band tail is defined symmetrically:

$$N_C(E) = N_{0,C} \exp[-(E_C - E)/E_U] \quad (E < E_C) \tag{12}$$

The valence and conduction band tails were varied together in the parametric study. The tail states are treated as distributed electronic states rather than as discrete defects associated with a specific atomic configuration, and their electron and hole capture cross-sections are specified independently.

The specific parameters used to model these electronic states are summarized in the following tables. Table 2 details the energy levels (E_t), capture cross-sections $(\sigma_{n,p})$, and densities (N_t) for both the discrete point defects and the exponential band tail distributions. In addition, the electronic properties of the Sb_2Se_3/CdS heterojunction, including the interface defect density and surface recombination velocities, are presented in Table 3.

The solar cell parameters listed in Table 1 were taken from the experimental data of the record Sb_2Se_3 reported by Zhao [9] and from previous SCAPS-1D studies on Sb_2Se_3 devices [26,28,30–35], and were kept fixed throughout this work. The defect model comprises bulk defects and band tail states in the absorber (Table 2) and defects at the CdS/Sb_2Se_3 interface (Table 3), with initial values based on references [30–35]. Urbach energy was obtained from the exponential sub-bandgap edge of the experimental EQE reported by Zhao [9], and the energy level of each defect was taken from Ref. [9]; both were kept fixed. The electron and hole capture cross sections and the total density of each defect were treated as free parameters and adjusted so that the simulated J-V and EQE responses reproduce the experimental data of the reference solar cell.

3. Results and discussion

3.1. Model validation

To establish a reliable basis for the sensitivity analysis, the model was at first calibrated against the experimental J-V and EQE characteristics of the record-efficiency Sb_2Se_3 solar cell reported by Zhao [9]. This step ensured that the effective one-dimensional device model, with the physical parameters defined in Section 2 and the defect-mediated recombination described above, reproduces the measured behavior of the reference solar cell.

Fig. 1a compares the simulated and experimental J-V characteristics under STC after the calibration process. The J-V agreement was quantified by MAE (0.547 mA cm^{-2}), RMSE (0.941 mA cm^{-2}), NMAE (1.26 %) and NRMSE (2.31 %), and the calibrated values of the free parameters are given in Tables 2 and 3 (Figs. S1 and S2). The simulated curve closely follows the experimental response across the entire voltage range. The extracted photovoltaic parameters summarized in Table 4 show relative deviations below 3 %. In particular, the close agreement in V_{oc} indicates that the selected defect energy levels and the back-contact work function are consistent with the measured device, although this agreement alone does not establish them uniquely. The extracted photovoltaic parameters summarized in Table 4 show relative deviations below 3 %. In particular, the close agreement in Voc indicates that the selected defect energy levels and the back contact work function are consistent with the measured solar cell, although this agreement alone does not establish them uniquely. Shifting each discrete defect level ± 0.05 changes the simulated J-V curve by less than 0.3 % (NRMSE), the interface defect being the most sensitive (Table S8).

The External Quantum Efficiency (EQE) comparison in Fig. 1b further supports the calibration. The simulated spectrum reproduces the experimental spectral response across the measured wavelength range. In the short-wavelength region (300 – 500 nm), the model captures the losses associated with parasitic absorption in the CdS window layer and the transmission of the front contact. In the long-wavelength region (600 – 1000 nm), the high EQE plateau is consistent with the absorption coefficient of Sb_2Se_3 [36,37] and with carrier diffusion lengths sufficient for efficient collection. The sub-bandgap response and the slope of the absorption edge near 1100 nm are reproduced by the EQE reported by Ref. [9]; the band tail states included in the model are electronic states and do not modify the optical absorption.

The simultaneous agreement in both J-V and EQE characteristics demonstrates that the numerical model with comprehensive defect configurations and specific material parameters captures the balance between photogeneration, bulk recombination, and interface losses in the Sb_2Se_3 solar cell stack. The model and simulation framework can therefore be considered a consistent effective representation of the Sb_2Se_3 heterojunction and a reliable basis for the defect sensitivity analysis, while the calibrated parameter set is the best fit within the explored parameter space rather than a unique solution.

Table 4
Comparison between experimental [9] and simulated J-V parameters.

Parameter	Experimental	Simulation	Relative Error
J_{sc} (mA·cm^{-2})	33.52	33.90	1.1 %
V_{oc} (mV)	467	471	0.9 %
FF (%)	67.64	65.68	2.9 %
η (%)	10.57	10.48	0.9 %

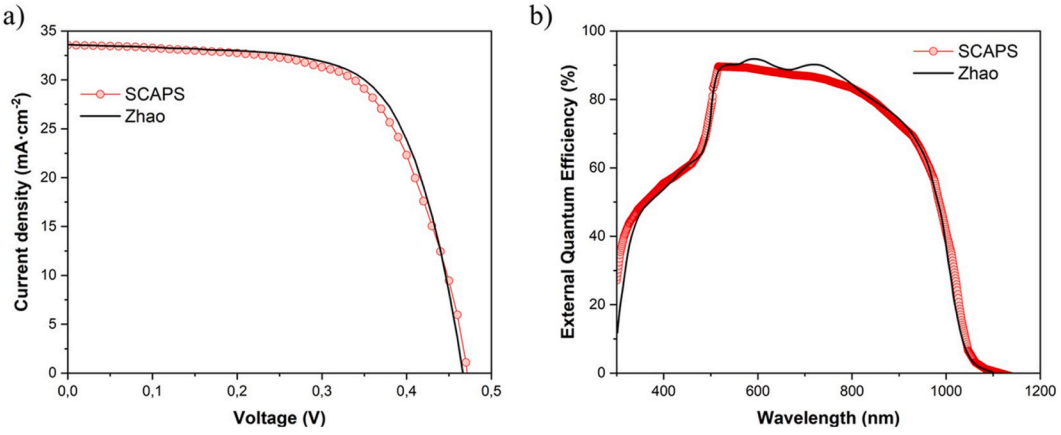


Fig. 1. Comparison of the a) J-V characteristics and b) External Quantum Efficiency (EQE) reported experimentally by Zhao [9] with those simulated with SCAPS-1D. J-V curves: AM1.5G illumination (100 mW cm^{-2}), T = 300 K. EQE: simulated at short circuit (V = 0).

3.2. Sensitivity analysis of defect states and recombination centers

To investigate the influence of intrinsic defects mechanisms on the optoelectronic performance of Sb_2Se_3, a simulation-based sensitivity analysis was conducted considering four defect classes (Table 2): a single acceptor, a single donor, a double donor, and exponential band tails. A full factorial design of experiments framework was employed to systematically evaluate both the individual and combined effects of these defect classes across all possible defect configurations. This approach enables quantitative assessment of the relative contribution and interaction of each defect type to the resulting electronic behavior. This section analyzes how these defects combinations modify the principal electronic performance indicators, including electrostatic profiles, recombination pathways, carrier transport limitations, and overall photovoltaic characteristics.

Fig. 2 shows the electric-field profiles across the Sb_2Se_3 absorber under AM1.5G illumination at short circuit (V = 0), with x measured from the rear contact (x = 0) to the CdS/Sb_2Se_3 junction (x = 1 μm); negative values correspond to a field driving electrons towards the CdS/Sb_2Se_3 junction. Four groups are distinguished. The defect-free case and all single donor/single acceptor combinations (black) retain a strong negative field localized at the junction. Configurations with band tails but without double donor (green) show a narrower junction field that preserves its polarity. Configurations combining the double donor and band tails (red) preserve a collection region of ~0.15 μm adjacent to the n-type layer, while the absorber bulk is quasi field-free with only a weak positive field. In contrast, configurations containing the double donor without band tails (blue) show field-polarity reversal in the ~0.4 μm adjacent to the junction, precisely where photogeneration is highest, while the main band bending is displaced towards the rear contact. Thus, the decisive difference is not the presence of a positive field per se, but its location relative to the photogeneration region.

In the absence of the double donor defect, all electric-field profiles retain a negative electric field at the junction, consistent with a p-type absorber and a conventional n-CdS/p-Sb_2Se_3 junction [15,19]. Single donor and single acceptor defects have a negligible effect on the field profile. Band tail states preserve the field polarity but narrow the depletion region, because the charge trapped in tail states increases the space-charge density adjacent to the junction. Since Urbach energy and carrier mobilities are fixed in the model, this effect is purely electrostatic and recombination-related, not a result of increased energetic disorder or mobility reduction.

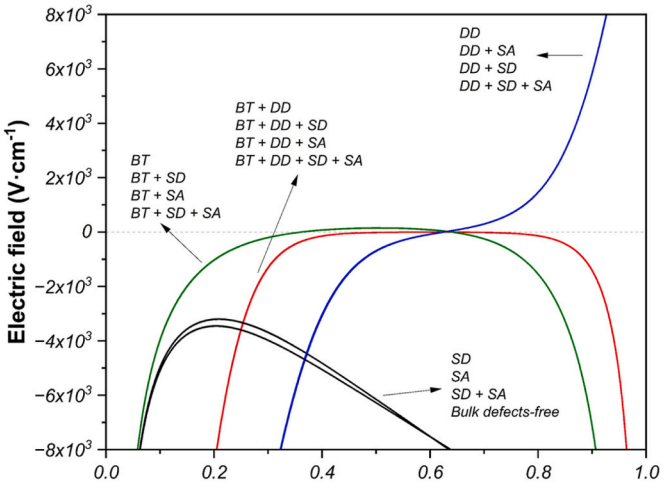


Fig. 2. Simulated electric field profiles across the Sb_2Se_3 absorber for all defect combinations, under AM1.5G illumination at V = 0 and T = 300 K. The coordinate x measured from the rear contact (x = 0) towards the CdS/Sb_2Se_3 junction (x = 1 μm). Negative values correspond to a field driving electrons towards the junction. Four distinct groups are identified: no bulk defects and single donor and single acceptor combinations (black), band tails without double donor (green), double donor with band tails (red), and double donor without band tails (blue). The double donor without band tails reverses the field polarity adjacent to the junction, whereas band tails narrow the junction field without changing its polarity and, when combined with the double donor, preserve the collecting front region.

The double donor produces the most pronounced electrostatic disruption [14–16]. To identify its origin, Fig. 3 compares the DD-only, BT-only and DD + BT configurations at short circuit: (a) energy band diagrams, (b) ionized defect charge density, (c) electron and hole current densities, and (d) electron and hole densities. In the DD-only solar cell, the ionized double donor charge exceeds the background acceptor density throughout the absorber. The absorber is thereby inverted to effectively n-type: electrons become the majority carriers in the bulk. The main band bending is relocated to the rear contact, and the bands bend upwards by ~0.14 eV towards the junction. The reverse front field drives holes towards the CdS/Sb_2Se_3 interface, producing a hole flux of ~35 mA cm^{-2} into the interface. There both carrier densities reach ~10^{13} cm^{-3}, compared with 2 × 10^{10} cm^{-3} in the other two configurations, which maximizes interface recombination.

When band tails are also present, the tail states supply a large negative space charge in the front region, virtually identical to that of the BT-only solar cell. This charge sustains the junction field irrespective of the double donor. In the bulk, the net defect charge remains of the order of N_A, so the absorber stays p-type, albeit with a lower hole density than in the BT-only solar cell. Consequently, in both BT-only and DD + BT, photogenerated holes are transported as majority carriers to the rear contact, and electrons are collected at the junction.

The current-loss budget at short circuit (Table 5) quantifies these mechanisms. In the DD-only solar cell, 35.8 of the 38.8 mA cm^{-2} generated are lost to interface recombination, whereas bulk SRH recombination accounts for only 0.99 mA cm^{-2}. In the BT-only and DD + BT solar cells, interface recombination is negligible (~0.01 mA cm^{-2}). The collapse of J_{sc} in all double donor configurations without band tails (Table 6) therefore originates from the loss of the collecting front field and the resulting interfacial recombination, not from bulk recombination.

Table 6 summarizes the simulated photovoltaic parameters for all defect configurations considered in combinatorial design of experiments. The macroscopic device response is interpreted in conjunction with the electric field profiles (Fig. 2), quasi-Fermi level splitting (Fig. 4) and spatial SRH recombination rate (Fig. 5). The configuration without bulk defects establishes the upper performance limit of the simulated device, yielding η = 15.42 %. Configurations containing only isolated single donor (SD) and/or single acceptor (SA) defects exhibit virtually identical photovoltaic parameters, confirming that these point defects exert only a negligible influence on the electrostatic and recombination landscape of the device.

A completely different behavior emerges in the presence of double donor (DD) defects. Independently of the coexistence of SD or SA, all DD-only configurations exhibit an almost complete collapse of photovoltaic operation, with efficiencies below 0.5 %. This severe degradation originates from the strong built-in field inversion previously identified in Fig. 3, which drastically suppresses carrier collection and transport across the absorber. Interestingly, despite this catastrophic reduction in current extraction, the simulated V_{oc} remains relatively high. This apparent decoupling indicates that the dominant effect of isolated double donor defects is not a direct collapse of the carrier chemical potential separation, but rather a severe electrostatic disruption of the junction. The relatively preserved quasi-Fermi level splitting further confirms that thermodynamic losses alone cannot explain the extreme performance degradation induced by isolated double donor states.

Band tail (BT) states produce a distinct degradation regime. In all band tail containing configurations excluding isolated double donor dominance, V_{oc} decreases systematically, accompanied by moderate reductions in J_{sc} and FF, leading to efficiencies near 10-11 %. Unlike the double donor-dominated regime, the degradation associated with band tail states remains relatively balanced across all photovoltaic parameters.

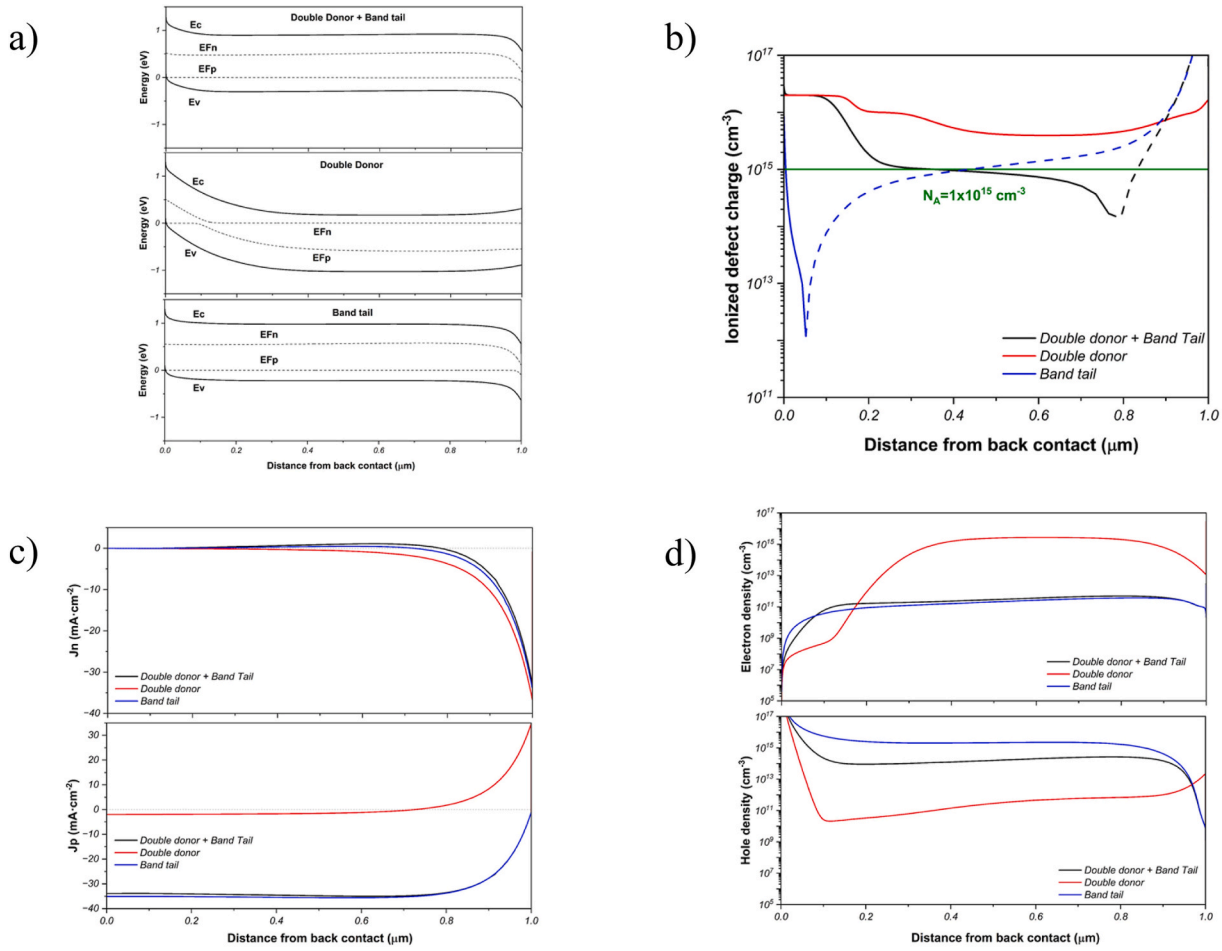


Fig. 3. Solar cell electrostatics and transport at short circuit (V = 0, AM1.5G) for the DD-only, BT-only and DD + BT configurations. (a) Energy band diagrams with electron and hole quasi-Fermi levels; (b) ionized defect charge density (solid: positive; dashed: negative; horizontal line: background acceptor density N_A); (c) electron and hole current densities; (d) electron and hole densities.

Table 5
Current-loss budget at short circuit (V = 0, AM1.5G). All values in mA·cm^{-2}.

	DD	BT	DD + BT
J_{gen}	38.8	38.8	38.8
Bulk SRH (absorber)	0.99	3.61	4.87
CdS/Sb_2Se_3 interface	35.8	~0.01	~0.01
J_{sc}	1.97	35.09	33.90

This behavior is fully consistent with the quasi-Fermi level splitting analysis, where band tail-containing configurations systematically exhibit lower $E_{Fn} - E_{Fp}$ values and stronger spatial non-uniformity near the interface. These results identify the density of band tail states as the main bulk voltage-limiting mechanism in the simulated device. The systematic reduction of V_{oc} observed in all band tail-containing configurations strongly suggests that band tail states constitute one of the principal origins of the characteristic V_{oc} deficit widely reported in Sb_2Se_3 solar cells, together with interface recombination. From a materials perspective, these results indicate that the density of localized band tail states plays an important role in the recombination losses that limit the solar cell open-circuit voltage. Urbach energy was kept fixed (Table 2) in the present simulations, a value obtained from the exponential sub-bandgap edge of the experimental EQE of the reference solar cell reported by Zhao [9], which the model aims to reproduce, and assumed equal for the electronic tail states in the simulations. Therefore, the observed variations in photovoltaic performance are attributed to changes in the density of band tail states and not changes in the energetic broadening of the band edges.

Table 6
Comparison of J-V parameters as function of the combination of defects simulated.

	J_{sc} (mA·cm^{-2})	V_{oc} (mV)	FF (%)	η (%)
No bulk defects	38.25	524.47	76.81	15.42
Single donor (SD)	38.25	524.75	76.81	15.42
Double donor (DD)	1.97	551.66	44.26	0.48
Single acceptor (SA)	38.27	524.39	76.94	15.44
Band tails (BT)	35.09	468.47	67.30	11.06
SD + DD	1.97	551.64	44.25	0.48
SD + SA	38.27	524.41	76.94	15.44
SD + BT	35.09	468.47	67.30	11.06
DD + SA	1.98	551.27	44.23	0.48
DD + BT	33.90	470.61	65.68	10.48
SA + BT	35.09	468.45	67.30	11.06
SD + DD + SA	1.98	551.24	44.23	0.48
SD + DD + BT	33.90	470.61	65.68	10.48
SD + SA + BT	35.09	468.45	67.30	11.06
DD + SA + BT	33.90	470.60	65.68	10.48
SD + DD + SA + BT	33.90	470.60	65.68	10.48

The coexistence of double donor and band tail defects produces a hybrid degradation regime governed simultaneously by electrostatic perturbation and band tail recombination [44]. While isolated double donor defects alone nearly suppress current extraction completely, the simultaneous introduction of band tail states partially restores photovoltaic operation, increasing J_{sc} and improving overall efficiency to approximately 10.5 %. Nevertheless, the recovered device remains strongly voltage-limited, with

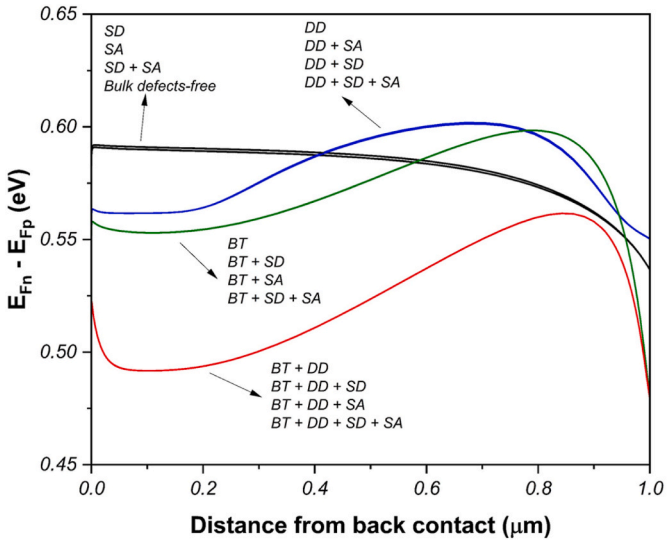


Fig. 4. Simulated quasi-Fermi level splitting $(E_{Fn} - E_{Fp})$ across the Sb_2Se_3 absorber for all defect combinations, under AM1.5G illumination at open circuit and T = 300 K. The coordinate x is measured from the rear contact (x = 0) towards the CdS/Sb_2Se_3 junction (x = 1 μm). Four groups are identified, with band tails emerging as the dominant voltage-limiting defect species and the double donor does not reduce the splitting; in the absence of band tails, it inverts the absorber to n-type, so the local splitting no longer maps onto V_{oc} in the same way.

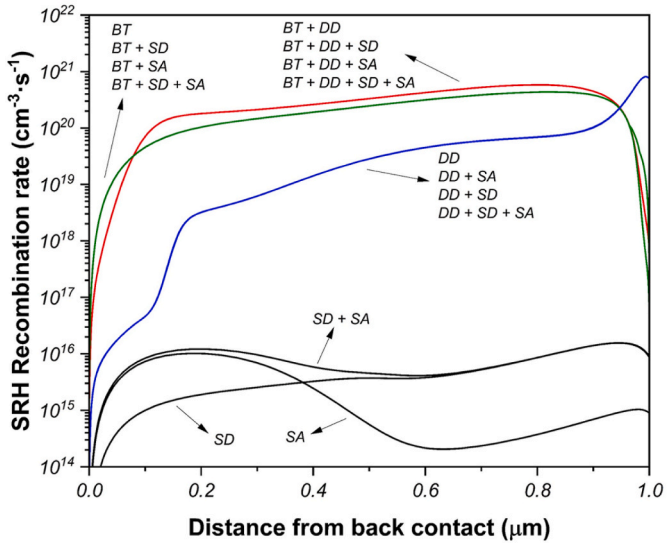


Fig. 5. Simulated SRH recombination rate across the Sb_2Se_3 absorber for all defect combinations, under AM1.5G illumination at short circuit (V = 0, T = 300 K). The coordinate x is measured from the rear contact (x = 0) towards the CdS/Sb_2Se_3 junction (x = 1 μm).

V_{oc} stabilized near 470 mV. This non-linear behavior demonstrates that the combined defect response cannot be interpreted through simple additive superposition. Instead, band tail states modify the electrostatic and recombination landscape induced by double donor defects, partially mitigating the extreme transport suppression associated with isolated field inversion while simultaneously maintaining strong recombination-driven voltage losses. The resulting operating regime therefore reflects the transition from an idealized absorber toward a realistic defect-limited Sb_2Se_3 solar cell.

The addition of single donor and single acceptor defects to double donor combined band tail configurations produces virtually no further variation in photovoltaic response. This confirms that the global device behavior is overwhelmingly controlled by the interplay between double donor and band tail states, while isolated single donor and single acceptor remain electrically secondary despite their likely presence in realistic absorbers.

The macroscopic photovoltaic response is consistent with the defect-dependent mechanisms identified in the microscopic analysis. Under the parameter set adopted for the reference device, double donor defects produce the largest changes in the electrostatic field and carrier-extraction profiles, whereas band tail disorder has a strong influence on the quasi-Fermi level splitting and the associated V_{oc} deficit. The combined effects of these defect populations therefore provide a consistent explanation for the simulated photovoltaic losses in the considered device.

The DD-BT interaction is therefore not beneficial per se. Band tails suppress the electrostatic failure mode of the double donor, leaving only its recombinative contribution. The additional bulk SRH current in DD + BT relative to BT-only quantitatively accounts for the J_{sc} difference between the two configurations. The single acceptor, despite its negative charge, does not restore the device (Table 6), because its density is much lower than that of the double donor. Compensation requires a negatively charged population comparable to the ionized double donor charge, which the band tail density of states provides. These findings should be interpreted as a device-specific result rather than as an intrinsic hierarchy of defect types: whether the double donor inverts the absorber depends on its density relative to N_A and to the negative charge that tail states can accommodate under the adopted defect parameters.

Fig. 4 shows the spatial distribution of the quasi-Fermi level splitting across the Sb_2Se_3 absorber at open circuit for all defect combinations, which fall into the same four groups as in Fig. 2. The configuration without bulk defects and all single donor and single acceptor combinations (black) exhibit a nearly uniform splitting of ~0.59 eV that decreases slightly towards the front interface, confirming that these point defects have only a minor influence on the electronic quality of the absorber.

The double donor without band tails (blue) does not reduce the splitting. It decreases slightly near the rear contact, to ~0.56 eV, but rises above that of the device without bulk defects in the central and front regions, up to ~0.60 eV, consistent with the slightly higher V_{oc} of these configurations (Table 6). Since the double donor inverts the absorber to n-type, the local splitting no longer maps onto V_{oc} in the same way, and the collapse of these devices originates in carrier collection rather than in a loss of quasi-Fermi level splitting.

Band tails without the double donor (green) reduce the splitting in the rear half of the absorber, to ~0.55 eV, where recombination through tail states depletes the electron population, whereas it recovers towards the front region. When band tails and the double donor coexist (red), the splitting is the lowest across most of the absorber, falling to ~0.49 eV near the rear contact and to ~0.48 eV at the front interface, close to the device V_{oc}. In this configuration the double donor only adds bulk recombination (Table 5), which lowers the splitting in the bulk but leaves V_{oc} essentially unchanged with respect to band tails alone, because V_{oc} is set at the front interface, where interface recombination dominates near open circuit. Band tails are therefore the only bulk defect species that reduce V_{oc} [44,45] in this parameter set.

To locate the non-radiative losses, Fig. 5 shows the bulk SRH recombination rate across the absorber at short circuit for all defect combinations. The integrated losses for the DD-only, BT-only and DD + BT configurations, including interface recombination, are given in Table 5. Four regimes are identified, mirroring the electrostatic groups of Fig. 2. In configurations with band tails but without the double donor, bulk SRH recombination increases from the rear contact towards the junction and drops within the junction depletion region. Since $p \gg n$ in the bulk, recombination through tail states is limited by the electron density, which increases towards the front, where photogeneration is highest. Because Urbach energy and carrier mobilities are fixed, this reflects recombination through tail states rather than reduced mobility or increased

disorder. The integrated bulk loss amounts to 3.61 mA cm^{-2}.

Configurations combining band tails and the double donor show the same profile shape, with higher rates throughout the absorber. In this regime the absorber remains p-type and the junction field is preserved (Fig. 3), so the double donor acts only as an additional bulk recombination center. The integrated bulk loss increases to 4.87 mA cm^{-2}, an increase of 1.26 mA cm^{-2} that accounts for most of the J_{sc} difference relative to the band tail only configuration (Table 5). Double donor configurations without band tails show bulk SRH rates about one order of magnitude lower over most of the absorber, with a sharp peak within ~50 nm of the interface. This peak arises where the reversed front field drives holes towards the junction and $n \approx p$. The integrated bulk loss is only 0.99 mA cm^{-2}: the dominant loss in this regime is interface recombination, which is not captured by the bulk profile. The defect-free, single donor and single acceptor configurations exhibit minimal SRH activity, consistent with their near-ideal field profiles and quasi-Fermi level splitting.

Bulk recombination is therefore dominated by band tails, which are also the only bulk defect species that reduce V_{oc} (Table 6). The role of the double donor is primarily electrostatic. Without band tails, it causes the collapse of J_{sc} through field reversal and interface recombination, while V_{oc} is not degraded. With band tail present, it only adds bulk recombination and leaves V_{oc} essentially unchanged. Near open circuit, however, the dominant recombination channel is the CdS/Sb_2Se_3 interface (Section 4.4). This interpretation is specific to the solar cell conditions considered and should not be taken as a general hierarchy of degradation mechanisms in Sb_2Se_3 solar cells.

3.3. Defect density threshold and impact on photovoltaic performance

Building on these findings, this section focuses on the two dominant defect species and systematically examines the effect of their density (N_t). First, the DD and BT defects were evaluated independently by varying N_t over twelve levels from 1×10^{13} cm^{-3} to 1×10^{17} cm^{-3} (Figs. 6 and 7), complemented by the denser threshold sweeps described in Section 2.2. Their combined effect was then investigated using a 13×13 concentration matrix. In this matrix, the DD and BT concentrations were independently varied over 13 logarithmically spaced levels from 1×10^{14} to 1×10^{18} cm^{-3}, resulting in 169 SCAPS simulations. This sequential approach first established the individual concentration-dependent effects and then examines their combined influence, with particular attention to critical defect density thresholds and the interaction between the two loss mechanisms.

The optical absorption coefficient $(\alpha(\lambda))$, was defined from literature [36,37] and kept constant for all simulations. Therefore, the variation of the band tail state density does not modify the optical absorption spectrum or the absorption edge in the present model. The band tail states are introduced as electronic defect distributions and their effect is evaluated through the resulting recombination, charge distribution, quasi-Fermi level splitting, and photovoltaic response. Consequently, any changes in J_{sc}, V_{oc} or FF with increasing N_t are not attributed to a modification of the optical coefficient.

The four physical quantities evolve consistently with increasing double donor concentration (N_{DD}), validating the electrostatic and recombination mechanisms identified in the preceding combinatorial sensitivity analysis. At low defect concentrations, the electric field retains the characteristic negative profile expected for a conventional p-type Sb_2Se_3 absorber

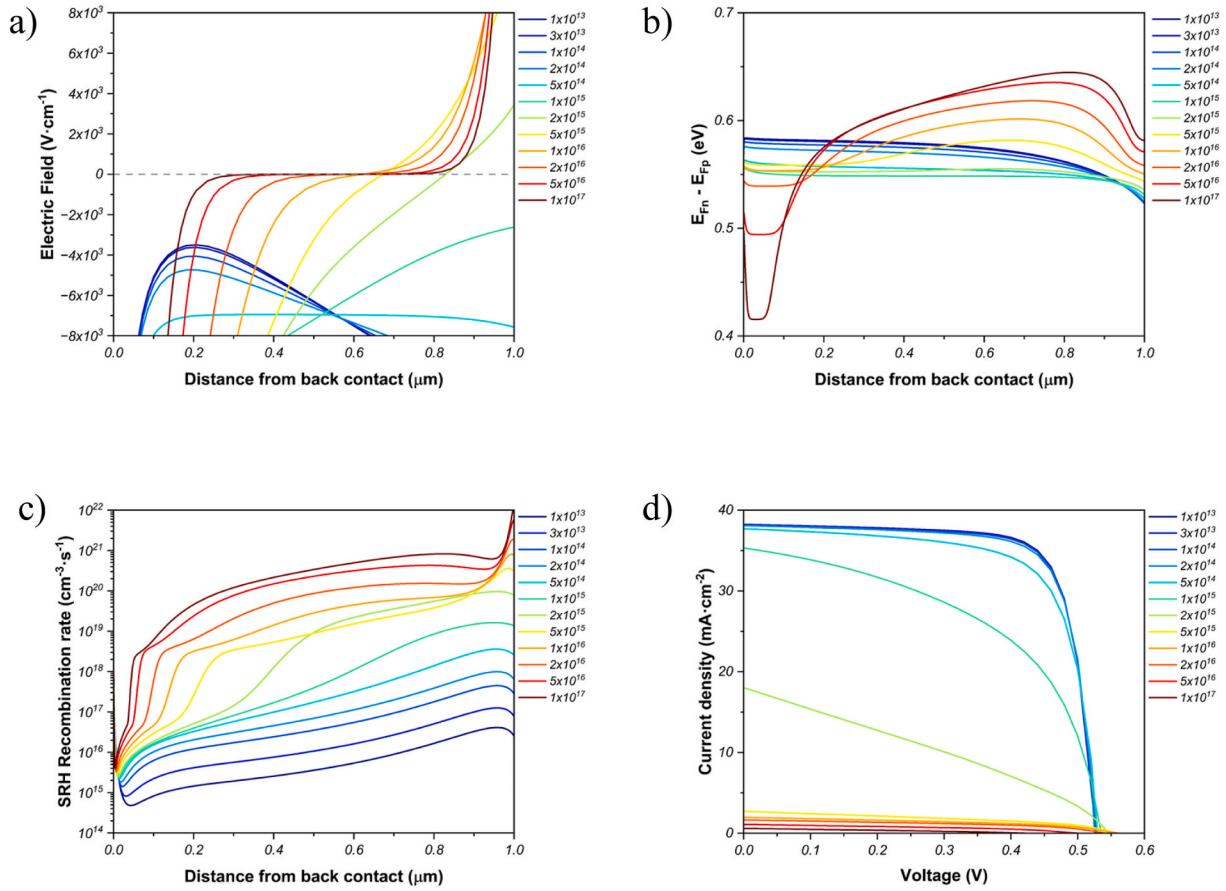


Fig. 6. Simulated a) electric field profile, b) quasi-Fermi level splitting, c) bulk SRH recombination rate, and d) J-V characteristics of the solar cell with the double donor defect as the only bulk defect, as a function of defect density N_{DD}. All simulations under AM1.5G illumination (T = 300 K). Profiles in a) and c) at short circuit and in b) at open circuit. Coordinate and sign conventions as in Fig. 2.

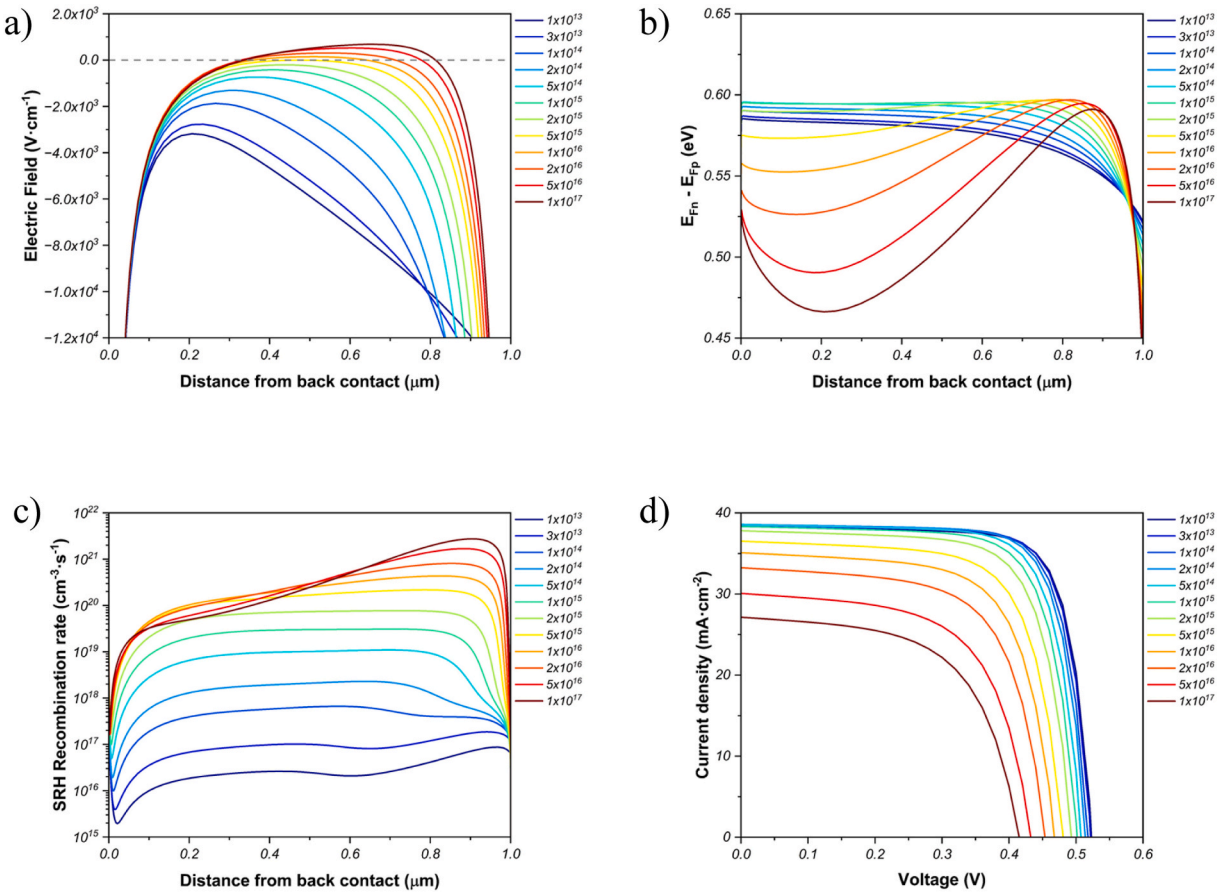


Fig. 7. Simulated a) electric field profile, b) quasi-Fermi level splitting, c) bulk SRH recombination rate, and d) J-V characteristics of the solar cell with band tail states as the only bulk defect, as a function of defect density N_t. All simulations under AM1.5G illumination (T = 300 K). Profiles in a) and c) at short circuit and in b) at open circuit. Coordinate and sign conventions as in Fig. 2.

(Fig. 6a). Since each double donor can carry two positive charges and the absorber is depleted of holes, the bulk space charge is approximately $q(N_{DD^+} + 2N_{DD^{2+}} - N_A) \approx q(2N_{DD^+} - N_A)$ for full ionization. For $N_{DD} < 5\times 10^{14}\ cm^{-3}$ the net charge remains negative, and the interface field decreases only from -1.2×10^4 to $-7.6 \times 10^3\ V{\cdot}cm^{-1}$ (Table S3). At $N_{DD} \approx N_A/2$ the bulk becomes nearly charge-neutral, and the field is approximately uniform. Above this value the positive double donor charge progressively weakens the junction field, which changes sign at $N_{DD} \approx 1.3 \times 10^{15}\ cm^{-3}$. This transition occurs under the adopted absorber doping $(N_A = 1 \times 10^{15}\ cm^{-3})$ and defect parameters used in the present simulations and should not be interpreted as a universal DD concentration threshold for Sb_2Se_3; since it is set by the condition $2N_{DD} \approx N_A$, it is expected to scale with the absorber doping. Consequently, the built-in field weakens across the absorber bulk. For $N_{DD} \geq 2 \times 10^{15}\ cm^{-3}$ the field is reversed over the front 0.17-0.4 μm of the absorber, adjacent to CdS/Sb_2Se_3 junction, so that holes are driven towards the interface, indicating severe electrostatic destabilization of the junction, and for $N_{DD} \geq 5\times 10^{15}\ cm^{-3}$ a quasi-neutral n-type region with near-zero field develops in the center of the layer (Fig. S3). The thermodynamic consequence of this electrostatic perturbation is reflected in the quasi-Fermi level splitting profiles (Fig. 6b). At low defect concentration, $E_{Fn} - E_{Fp}$ remains relatively uniform throughout the absorber, with values close to 0.58 eV. With increasing N_{DD}, the splitting rises in the central and front regions of the absorber, up to ≈0.65 eV, consistent with the slight increase in V_{oc} (Fig. 6d), whereas it drops sharply near the rear contact, falling below 0.45 eV for the highest simulated concentration. This strong spatial asymmetry indicates that the double donor does not produce a homogeneous thermodynamic degradation across the absorber volume. Since the splitting is evaluated at open circuit, where no current is extracted, it does not reflect the collection loss: the degradation of the solar cell originates in carrier collection rather than in the loss of quasi-Fermi level splitting.

The redistribution of recombination is directly reflected in the SRH recombination profiles shown in Fig. 6c. The recombination rate increases systematically with increasing N_{DD}, spanning more than five orders of magnitude. At high concentrations, the recombination rate rises steadily across the central and front regions of the absorber, reaching values close to $10^{21}\ cm^{-3}\ s^{-1}$ and exceeding them at the front interface. This behavior is consistent with the presence of the deep double donor level located near midgap (0.55 eV below Ec), which acts as an efficient trap-assisted recombination center according to Shockley-Read-Hall statistics. Simultaneously, the field suppression and redistribution of carriers associated with high N_t further enhance recombination activity near the junction. Nevertheless, at short circuit the integrated bulk SRH current remains around 1 mA cm^{-2} or below up to $N_{DD} \approx 10^{16}\ cm^{-3}$, whereas interface recombination rises from 0.5 to 36 mA cm^{-2} across the transition. The photocurrent loss is therefore dominated by holes reaching the CdS/Sb_2Se_3 interface rather than by bulk SRH.

The electrical impact of these microscopic perturbations is reflected in the simulated J-V characteristics (Fig. 6d). At low defect concentrations, the solar cell maintains near-ideal photovoltaic behavior, with J_{sc} values close to 38 mA cm^{-2} and only minor variations in V_{oc} and FF. However, once the double donor concentration approaches the electrostatic transition threshold $(\approx 10^{15}\ cm^{-3})$, the solar cell undergoes an abrupt degradation dominated by photocurrent loss. J_{sc} decreases by 10 % at $N_{DD} \approx 1.1 \times 10^{15}\ cm^{-3}$ and by 50 % at $1.9 \times 10^{15}\ cm^{-3}$, and the efficiency falls from 90 % to 50 % of its defect-free value within 0.36 decades (Fig. S4, Table S4). This collapse indicates severe suppression of carrier

extraction under disrupted junction-field conditions. In contrast, V_{oc} remains comparatively stable, increasing slightly to ~555 mV during the transition and decreasing only above $\approx 5 \times 10^{16}\ cm^{-3}$. This asymmetric degradation demonstrates that the isolated double donor primarily acts as an electrostatic and transport-disrupting defect rather than as a purely voltage-limiting recombination center. The dominant failure mechanism is therefore associated with undesired carrier collection losses induced by field suppression and junction destabilization.

Overall, this concentration-dependent analysis establishes a critical defect threshold near $10^{15}\ cm^{-3}$, at which $2N_{DD}$ exceeds N_A and the junction field reverses, beyond which electrostatic control of the junction rapidly collapses. These results confirm that double donor defects govern the electrostatic stability and carrier extraction capability of the simulated Sb_2Se_3 solar cell. To contrast this behavior, the following section applies an equivalent sensitivity analysis to band tail states, which were previously identified as the principal bulk voltage-limiting defect operating through bulk recombination rather than electrostatic compensation. Comparing these isolated concentration-dependent responses provides the physical basis required to interpret the complex degradation regime that emerges when both defect classes coexist simultaneously.

An equivalent concentration-dependent sensitivity analysis was performed for band tail states alone, with N_{BT} varied from 10^{13} to 10^{17} cm^{-3} in the absence of double donor defects. Originating from structural disorder in the Sb_2Se_3 absorber, band tail states introduce a continuous exponential distribution of localized states near the band edges. The evolution of the electric field, quasi-Fermi level splitting, SRH recombination rate, and J-V characteristics (Fig. 7) reveals a degradation mechanism fundamentally distinct from that induced by isolated double donor defects, particularly in its spatial distribution and thermodynamic impact.

The electric profiles shown in Fig. 7a show a gradual electrostatic response to increasing band tail disorder. At low defect concentrations, the field remains negative across the absorber, consistent with a conventional p-type absorber. As N_{BT} increases, the negative charge trapped in tail states accumulates near the junction, narrowing the depletion region, and the absorber bulk becomes quasi-field free. At the highest densities, a weak positive field appears in the bulk. Unlike the double donor, band tail states do not invert the absorber. Their negative charge reinforces its p-type character, and the junction field retains its polarity at all densities. Consistently, interface recombination at short circuit decreases from 0.36 to 2×10^{-3} mA cm^{-2} across the sweep (Table S5), as the reinforced junction field keeps holes away from the CdS/Sb_2Se_3 interface.

The quasi-Fermi level splitting profiles at open circuit (Fig. 7b) show the corresponding voltage loss. At low densities, $E_{Fn} - E_{Fp}$ remains nearly uniform, at ~0.59 eV. With increasing N_{BT}, a broad minimum develops in the rear half of the absorber, where the splitting decreases to ~0.47 eV at the highest densities, while it largely recovers towards the front region. Since generation is concentrated near the front, the shortened diffusion length associated with recombination through tail states (Fig. 7c) depletes the electron population in the rear region and reduces the local splitting there. At open circuit, qV_{oc} corresponds to the separation between the quasi-Fermi levels at the front and rear contacts, and the splitting profiles identify where this separation is reduced within the absorber. Together, these results account for the progressive V_{oc} loss with increasing band tail density.

Recombination progressively increases toward the front region of the absorber, particularly at high concentrations, reflecting the gradual suppression of efficient drift-assisted carrier extraction under weakened internal electric-field conditions. This broad volumetric recombination behavior confirms that band tail states operate through recombination distributed across the tail state distribution rather than through isolated deep recombination centers. At short circuit, the integrated bulk SRH current increases from 5×10^{-4} to 11.6 mA cm^{-2} across the sweep and accounts for the entire J_{sc} loss. These microscopic perturbations translate directly into the macroscopic J-V characteristics shown in Fig. 7d. Increasing band tail concentration progressively degrades all photovoltaic parameters: V_{oc} and FF decrease from the lowest densities, whereas J_{sc} is affected only above $\approx 5 \times 10^{15}\ cm^{-3}$. While low defect concentrations preserve near-ideal device performance, increasing N_t to 10^{17} cm^{-3} reduces V_{oc} to approximately 415 mV and decreases J_{sc} to 27 mA cm^{-2}. Unlike the severe transport collapse induced by isolated double donor defects, the band tail-induced degradation remains gradual and does not produce S-kink distortions in the J-V curves, consistent with the absence of complete junction inversion. No threshold is observed: the efficiency decreases from 90 % to 50 % of its defect-free value between $N_{BT} = 1.2 \times 10^{15}\ cm^{-3}$ and $5.8 \times 10^{16}\ cm^{-3}$, a transition of 1.7 decades compared with 0.36 decades for the double donor. Using the same criteria, J_{sc} decreases by 10 % at $N_{BT} = 1.3 \times 10^{16}\ cm^{-3}$ and efficiency by one absolute point at $6.5 \times 10^{14}\ cm^{-3}$.

The concentration-dependent band tail analysis establishes a degradation mechanism fundamentally different from that of double donor defects. Whereas double donor states destabilize the junction primarily through abrupt electrostatic compensation and the resulting carrier extraction failure, band tail states progressively reduce device performance through distributed volumetric recombination and the associated suppression of the quasi-Fermi level splitting. This distinction provides the physical basis required to understand the hybrid degradation regime observed when both defect classes coexist simultaneously in realistic Sb_2Se_3 solar cells.

To investigate their simultaneous impact, a comprehensive combinatorial sensitivity analysis was performed by independently varying the concentrations of both defect species. This approach enables direct visualization of their coupled influence on device performance and identifies the operational regimes where their interaction dominates the photovoltaic response.

The contour maps presented in Fig. 8 illustrate how double donor and band tail defects jointly govern the macroscopic photovoltaic parameters. Each map exhibits a distinct topology in the $N_{DD} \times N_{BT}$ parameter space, reflecting the interplay between electrostatic disruption and thermodynamic degradation. The interaction between DD and BT concentrations was quantified using a second-order response-surface model applied to 13×13 matrix [46]. For each photovoltaic response, the model was defined as:

$$\begin{aligned} Response = {} & \beta_0 + \beta_1 \log_{10}(N_{BT}) + \beta_2 \log_{10}(N_{DD}) \\ & + \beta_3 \log_{10}(N_{BT}) \log_{10}(N_{DD}) + \\ & + \beta_4 \left[\log_{10}(N_{DD})\right]^2 + \beta_5 \left[\log_{10}(N_{BT})\right]^2 \end{aligned} \tag{13}$$

where N_{BT} and N_{DD} are the band tail and double donor concentrations, respectively. The coefficient β_3 represents the DD×BT interaction term.

The J_{sc} map (Fig. 8a) exhibits a characteristic L-shaped degradation boundary. J_{sc} remains close to the ideal value when the double donor density remains below approximately 10^{15} cm^{-3} and the band tail density below approximately 10^{16} cm^{-3}. However, increasing either defect density beyond these values progressively suppresses carrier extraction. High double donor concentrations produce the most abrupt degradation, driving J_{sc} toward near-zero values as the internal junction field collapses due to electrostatic compensation. In contrast, increasing band tail density induces a more gradual reduction in current collection, consistent with enhanced volumetric recombination and weakened drift-assisted transport. These results confirm that both defect classes act as major extraction-limiting mechanisms, although through fundamentally different physical pathways. The single defect sweeps clarify how the two defects interact. With band tail states at their calibrated density (10^{16} cm^{-3}), the double donor threshold shifts by more than an order of magnitude: relative to the device with band tails only, the efficiency decreases by one absolute point at $N_{DD} = 2.4 \times 10^{16}\ cm^{-3}$ and J_{sc} by 10 % at $N_{DD} = 3 \times 10^{16}\ cm^{-3}$, compared with 4×10^{14} and $1.1 \times 10^{15}\ cm^{-3}$ without band tails. The negative tail-state charge in the front region offsets the positive double

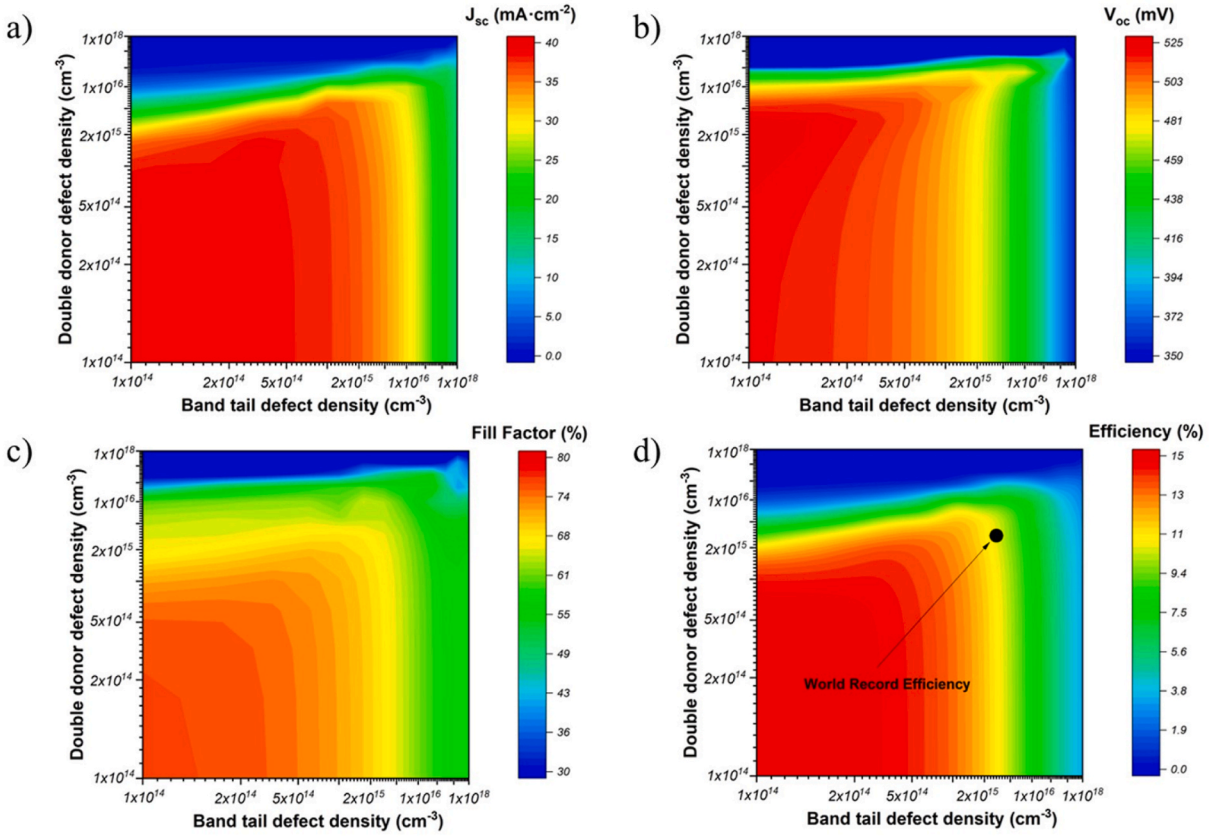


Fig. 8. Simulated contour maps of a) short-circuit current density J_{sc}, b) open-circuit voltage V_{oc}, c) fill factor FF, and d) power conversion efficiency as a function of double donor and band tail defect densities N_t. Maps interpolated in OriginPro (spline interpolation) from a 13×13 matrix of SCAPS-1D simulations; all 169 simulations converged. All simulations under AM1.5G illumination (T = 300 K).

donor charge and preserves the junction field up to double donor densities well above N_A, which produces the upward shift of the J_{sc} boundary at high band tail densities in Fig. 8a. Without band tails, $N_{DD} \approx 10^{16}\ cm^{-3}$ would reduce the efficiency to ~0.5 %.

The V_{oc} map (Fig. 8b) displays a markedly different topology, dominated primarily by the band tail concentration axis. At low-to-moderate double donor densities, V_{oc} decreases progressively with increasing band tail density, confirming that band tail recombination and quasi-Fermi level splitting suppression constitute the dominant voltage-limiting mechanism among the bulk defects. In the calibrated solar cell, V_{oc} is additionally limited by interface recombination, which dominates the recombination current near open circuit (Section 4.4). In contrast, isolated double donor defects alone exert comparatively limited influence on V_{oc} despite their undesirable impact on carrier extraction. V_{oc} decreases only at very high double donor densities (above $\approx 5 \times 10^{16}\ cm^{-3}$), where bulk SRH recombination becomes significant, and reaches its global minimum when both defect concentrations are high, reflecting the combination of electrostatic distortion and disorder-induced recombination. The FF map (Fig. 8c) exhibits intermediate behavior characterized by a diagonal degradation trend, indicating that FF is simultaneously sensitive to both defect classes.

The map of power conversion efficiency (Fig. 8d) integrates the combined impact of all degradation mechanisms. The high-efficiency region is confined to the low-defect-density corner of the parameter space, indicating that simultaneous suppression of both double donor and band tail defects is required to approach the intrinsic performance limit of the simulated architecture. The experimentally calibrated world record efficiency [9] "operating point" lies within an intermediate regime where both defect classes coexist at moderate concentrations, reproducing efficiencies close to 10.5 %. This agreement suggests that the record device operates in a co-limited regime controlled simultaneously by electrostatic instability, band tail recombination and interface recombination.

The response-surface analysis provides a quantitative assessment of the coupled effects observed in the contour maps. A statistically significant DD×BT interaction was obtained for efficiency, V_{oc}, J_{sc}, and FF, confirming that their combined response is not fully described by the independent effects of the two defect classes. The positive sign of all interaction coefficients indicates that band tail states attenuate the impact of double donors, although they themselves degrade the solar cell, consistent with the compensation of the double donor charge by the tail-state charge and the resulting shift of the double donor threshold. The interaction coefficients, 95 % confidence intervals, and p-values are summarized in Table 7, while the complete regression results are provided in Supporting Information Table S6.

Despite the record performance, the device reported by Zhao [9] still exhibits a significant V_{oc} deficit. To identify the origin of this limitation, the internal recombination and electronic profiles were examined. Fig. 9a shows the spatial distribution of the electron density and the Shockley-Read-Hall (SRH) recombination across the Sb_2Se_3 absorber. The electron density increases sharply within the first ~0.15 μm from the back contact and then remains relatively stable throughout most of the absorber bulk, reflecting the limited extension of the depletion region and the predominantly quasi-neutral p-type character of Sb_2Se_3. In parallel, the SRH recombination rate rises rapidly near the back contact and continues to increase gradually toward the front of the absorber, reaching $\sim 10^{20}\ cm^{-3}{\cdot}s^{-1}$ at ~0.85 μm, indicating that defect-assisted non-radiative recombination extends significantly into the absorber bulk rather than being exclusively interface-confined. Fig. 9b shows that the internal electric field is strongly localized near the front heterojunction and the back contact, while the majority of the absorber remains essentially field-free, with a positive field below $10^3\ V{\cdot}cm^{-1}$ between ~0.2 and 0.85 μm. Consequently, photogenerated minority carriers generated in the bulk must rely primarily on diffusion for

Table 7
Quantified DD-BT interaction from the second-order response-surface analysis of 169 SCAPS simulations. β(DD×BT) denotes the interaction coefficient and CI the 95 % confidence interval.

Response	R^2	Adjusted R^2	β (DD×BT)	95 % CI	p-value
Efficiency	0.789	0.782	1.086	0.865 – 1.308	7.38×10^{-18}
V_{oc}	0.605	0.592	14.330	6.434 – 22.227	4.48×10^{-4}
J_{sc}	0.733	0.725	2.202	1.519 – 2.886	1.88×10^{-9}
FF	0.662	0.652	1.340	0.361 – 2.320	7.59×10^{-3}

collection. Under such conditions, defect states, including deep-level donor antisite defects and band tail states, reduce the effective diffusion length through enhanced trap-assisted recombination, thereby limiting carrier extraction efficiency. The electrical manifestation of these loss mechanisms is shown in Fig. 9c, which compares the different recombination current components. Bulk recombination (J_{bulk}) dominates under short-circuit conditions, with $J_{bulk} = 4.9\ mA{\cdot}cm^{-2}$ and negligible interface recombination at V = 0, while interface recombination (J_{IFR}) increases exponentially with bias and becomes dominant near V_{oc}. The two components are comparable at the maximum power point (~0.37 V) and cross at ~0.40 V; at open circuit, interface recombination accounts for ~80 % of the total recombination current. Interface recombination is therefore the main factor constraining the achievable V_{oc}, as confirmed by the selective-reduction analysis in Section 4.4. Finally, the quasi-Fermi level splitting shown in Fig. 9d reflects the thermodynamic consequence of these recombination losses. The splitting reaches a maximum of ~0.56 eV at ~0.85 μm and decreases towards the front interface to ~0.48 eV, close to the device V_{oc}, consistent with the dominance of interface recombination near open circuit (Fig. 9c). A smaller reduction near the back contact, to ~0.49 eV, coincides with the region of low electron density in Fig. 9a.

Importantly, even the solar cell without bulk defects remains significantly below the Shockley-Queisser efficiency limit (32 %) [47] expected for a 1.1 eV absorber as used in this model. This indicates that bulk-defect recombination alone does not fully determine the solar cell efficiency limit. Additional limitations associated with interface recombination, heterojunction energetics, band alignment, carrier transport asymmetry, depletion width, and contact selectivity also contribute to constraining the achievable photovoltaic performance. Consequently, further efficiency improvements in Sb_2Se_3 solar cells will likely require simultaneous optimization of both absorber defect chemistry and overall device architecture.

4. Practical implications

The detailed analysis of recombination processes, electrostatic profiles, and carrier transport presented in the previous section provides a comprehensive framework for understanding and mitigating the performance limitations of Sb_2Se_3 thin-film solar cells.

These insights allow the formulation of a defect-tolerance roadmap

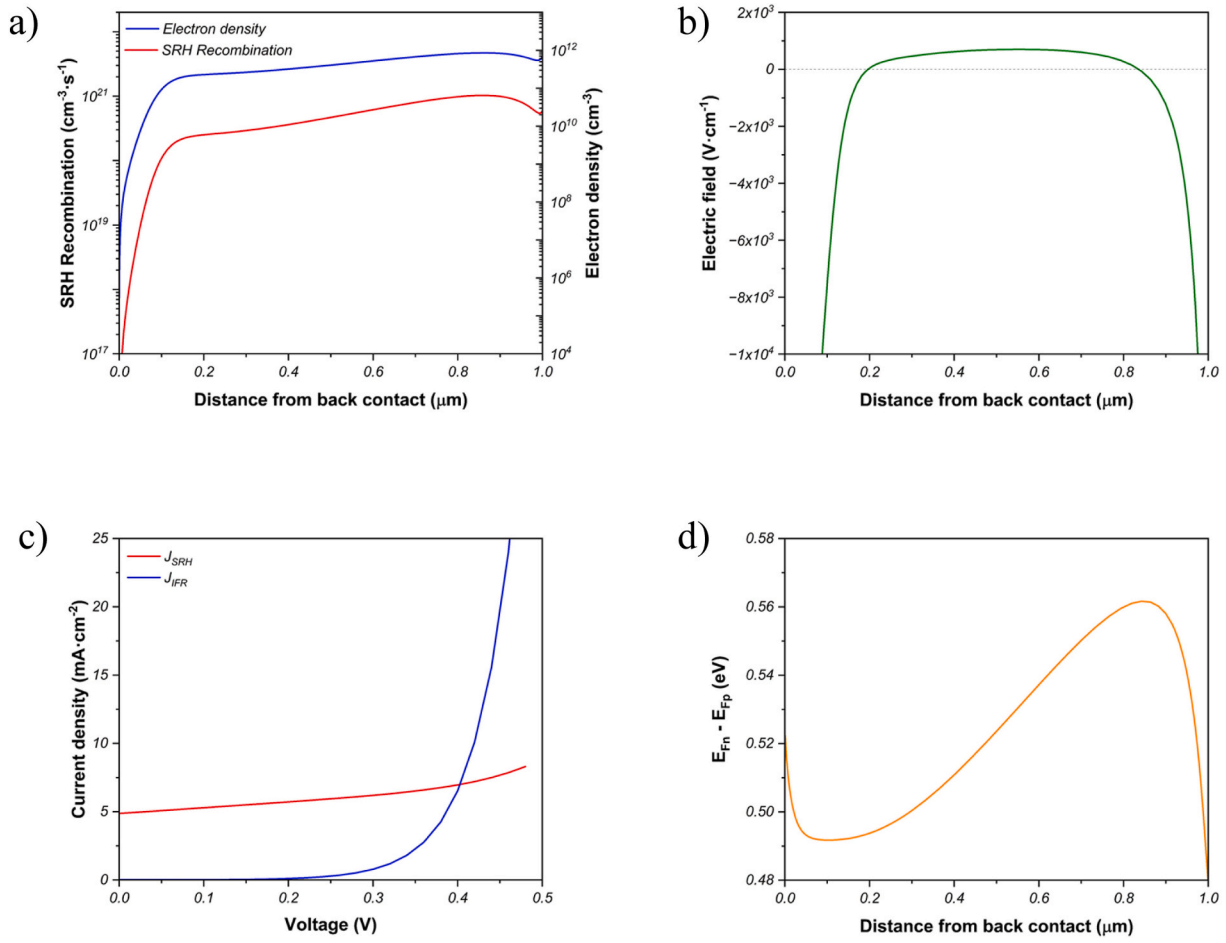


Fig. 9. Internal profiles of the calibrated Sb_2Se_3 solar cell under AM1.5G illumination (T = 300 K): a) electron density and bulk SRH recombination rate across the absorber at short circuit; b) electric field distribution at short circuit, with the detail of the quasi-field-free bulk region; c) bulk (J_{SRH}) and interface (J_{IFR}) recombination current components as function of applied voltage; and d) quasi-Fermi level splitting ($E_{Fn} - E_{Fp}$) across the Sb_2Se_3 layer at open circuit voltage. Coordinate and sign conventions as in Fig. 2.

for Sb_2Se_3 absorbers. Rather than all defects contributing equally to performance degradation, the results demonstrate that only a limited number of defect populations (two bulk defect families and the CdS/Sb_2Se_3 interface) determine the dominant loss mechanisms. Identifying these critical defect families and their associated tolerance thresholds provides practical guidance for material optimization and device engineering aimed at overcoming the current efficiency limitations of Sb_2Se_3 solar cells.

4.1. Experimental growth control

The two dominant defect families in the simulations, band tail states and double donor defects, are directly linked to the structural and compositional properties of Sb_2Se_3 thin films and therefore require distinct experimental mitigation strategies.

Band tail states are commonly attributed to structural disorder inherent to the quasi-one-dimensional $[Sb_4Se_6]_n$ ribbon lattice [48]. Grain boundaries, ribbon misorientation, lattice strain, and defective ribbon terminations can generate localized states extending from the band edges into the bandgap. Experimentally, the associated energetic disorder can be characterized through Urbach energy [44]. In the present simulations, Urbach energy was kept fixed at 0.032 eV (Table 2), obtained from the exponential sub-bandgap edge of the experimental EQE reported in Ref. [9], while the total density of band tail states was systematically varied. The simulations therefore isolate the effect of band tail state density on the recombination losses that progressively reduce V_{oc} and FF and, at high densities, J_{sc}. Strategies to improve absorber crystallinity, such as optimized nucleation, enlarged grain size, preferential [hk1] ribbon orientation, and post-annealing treatments, are expected to reduce the density of localized band tail states and, in turn, mitigate these losses. Such strategies may also narrow Urbach energy, an effect not captured in the present analysis.

The double donor-like response is commonly associated with Sb_{Se} antisites and related donor-type defect complexes favored under Se-poor growth conditions [17]. These defects introduce deep donor levels near 0.2 eV and 0.55 eV below Ec, acting simultaneously as electrostatic compensating centers and efficient SRH recombination sites. The simulations identified that the junction field reverses and carrier extraction collapses at $N_{DD} \approx 10^{15}\ cm^{-3}$ when the double donor is the only bulk defect, and above $\approx 2 \times 10^{16}\ cm^{-3}$ in the presence of band tail states. Suppressing these donor-like states therefore requires strict control of the Se/Sb stoichiometry during film growth. Moderately Se-rich deposition conditions, chalcogen-rich post-annealing treatments, and Se-containing additives can all help reduce the formation of selenium-deficient donor complexes.

Importantly, the simulations demonstrate that improving only one defect family is insufficient to achieve high-efficiency solar cells. Structural disorder control is necessary to minimize band tail-induced voltage losses, while stoichiometric control is simultaneously required to suppress double donor-induced electrostatic degradation. The order of these improvements also matters: because the negative tail-state charge offsets the positive double donor charge, reducing the band tail density without reducing the double donor density would remove this compensation and could trigger the collection collapse at the calibrated $N_{DD} \approx 10^{16}\ cm^{-3}$ (Fig. 8). This establishes a two-dimensional defect-control framework for further optimization of Sb_2Se_3 solar cells, to be combined with passivation of the CdS/Sb_2Se_3 interface.

4.2. Photovoltaic figures of merit

The simulations show that band tail states and double donor defects degrade photovoltaic performance through distinct mechanisms, although their combined effect is not additive, each affecting different figures of merit.

Among the bulk defects, band tail states mainly limit V_{oc} and FF. By introducing an exponential distribution of localized states near the band edges, they progressively suppress the quasi-Fermi level splitting and increase distributed non-radiative recombination. As band tail density increases, V_{oc} decreases systematically from 524 mV at $10^{13}\ cm^{-3}$ to 415 mV at $10^{17}\ cm^{-3}$, FF decreases in parallel, and J_{sc} is reduced only above $\sim 5 \times 10^{15}\ cm^{-3}$ through enhanced bulk recombination. This identifies the density of localized band tail states as a major contributor to the characteristic V_{oc} deficit in Sb_2Se_3 solar cells, together with interface recombination, which dominates near open circuit in the calibrated solar cell. In contrast, double donor defects primarily degrade J_{sc} and FF through electrostatic destabilization of the junction. Both donor levels are ionized in the depleted absorber, so that the positive double donor charge, up to $2N_{DD}$, compensates the native p-type doping and reverses the junction field at $N_{DD} \approx 1.3 \times 10^{15}\ cm^{-3}$; the resulting collection loss is dominated by interface recombination rather than by bulk SRH through the deep level. Once this threshold is exceeded, carrier extraction collapses and J_{sc} rapidly approaches near-zero values. Despite this severe transport degradation, isolated double donor defects produce comparatively minor changes in V_{oc}, confirming that their dominant effect is electrostatic rather than thermodynamic. When both defects coexist, their interaction becomes strongly non-linear. The presence of band tail states partially mitigates the extreme transport collapse induced by isolated double donor defects, shifting the double donor threshold by more than an order of magnitude, but simultaneously maintains strong recombination-driven voltage losses, reproducing the experimentally calibrated regime near 10.5 % efficiency [9]. The results therefore indicate that, for the calibrated device, the difficulty in moving beyond the current 10-11 % efficiency plateau can be linked to defect-controlled bulk and interface recombination and electrostatic losses rather than intrinsic optical limitations [35]. Simultaneous suppression of both dominant defect types, together with interface passivation, is therefore required for further efficiency improvements.

4.3. Critical defect density thresholds

The simulations demonstrate that the defect-tolerance space for high performance Sb_2Se_3 solar cells is inherently two-dimensional, since device performance depends simultaneously on the concentrations of band tail states and double donor defects.

Band tail states induce a progressive and distributed degradation dominated by quasi-Fermi level splitting suppression. Increasing band tail density continuously reduces V_{oc} across the full simulated range, with the strongest losses above $\sim 10^{15}\ cm^{-3}$. At the highest concentrations, $10^{17}\ cm^{-3}$, V_{oc} decreases toward 415 mV while J_{sc} falls to 27 mA cm^{-2}. No critical threshold exists for this defect: the efficiency decreases from 90 % to 50 % of its value without bulk defects over 1.7 decades of band tail density and already falls by one absolute point at $\sim 6.5 \times 10^{14}\ cm^{-3}$. Because Urbach energy is fixed at 0.032 eV in these simulations, these results quantify specifically the effect of the band tail state density on solar cell performance. The results indicate that any reduction in the population of localized band tail states mitigates both the voltage and carrier-collection losses, so that the band tail density should be minimized rather than kept below a specific value.

In contrast, double donor defects exhibit a threshold-driven electrostatic degradation, whose origin was discussed in Section 3: when the ionized double donor charge, up to $2N_{DD}$, exceeds the background acceptor density, the junction field reverses and holes are driven to the CdS/Sb_2Se_3 interface, where they recombine. When the double donor is the only bulk defect, the efficiency falls by one absolute point at $N_{DD} \approx 4 \times 10^{14}\ cm^{-3}$, J_{sc} decreases by 10 % at $1.1 \times 10^{15}\ cm^{-3}$, and the whole transition occurs within 0.36 decades (Fig. S4 and Table 8). V_{oc} is not degraded within this range and decreases only above $\approx 5 \times 10^{16}\ cm^{-3}$, so that the dominant failure mode is a loss of carrier collection rather than an increase in recombination-limited voltage loss. Because this threshold is set by the condition $2N_{DD} \approx N_A$, it is specific to the adopted absorber doping and is expected to scale with it; it should not be

interpreted as a universal double donor threshold for Sb_2Se_3. The threshold also depends on the other bulk defects. With band tail states at their calibrated density, the negative tail-state charge offsets the double donor charge and shifts the threshold by more than an order of magnitude, to $\approx 2.4 \times 10^{16}\ cm^{-3}$ for a one-point efficiency loss and $\approx 3\times 10^{16}\ cm^{-3}$ for a 10 % J_{sc} loss, while the transition remains sharp. The calibrated record solar cell, with $N_{DD} = 1 \times 10^{16}\ cm^{-3}$, therefore operates only a factor of 2-3 below this shifted threshold, so that a moderate increase in double donor density, for example under Se-poor growth conditions, would trigger the collection collapse. These threshold densities are insensitive to the numerical mesh, with an uncertainty below 1 % (Table S2).

The efficiency contour maps directly reflect this two-dimensional tolerance space. The high-efficiency regime is confined to the low-defect-density region where both band tail and double donor concentrations remain simultaneously below their critical thresholds. Outside of this region, optimization of only one defect family cannot compensate for degradation induced by the other. Reducing band tail density alone reduces bulk recombination losses but not the extraction losses caused by double donor defects, and at double donor densities above $\approx 10^{15}\ cm^{-3}$ it can even trigger the collection collapse by removing the compensating tail-state charge; conversely, suppressing double donor defects alone cannot recover the thermodynamic voltage losses imposed by band tail states. The simulations demonstrate that simultaneous suppression of both dominant defect classes, together with passivation of the CdS/Sb_2Se_3 interface, is required to surpass the current efficiency plateau in Sb_2Se_3 solar cells.

4.4. Strategies for improving device performance

The simulation results provide guidelines for prioritizing experimental strategies towards high-performing Sb_2Se_3 solar cells. To prioritize these strategies quantitatively, Fig. 9c decomposes the recombination current of the reference solar cell into bulk and interface contributions (Table S7). At short circuit, recombination occurs almost entirely in the bulk $\left(J_{SRH} \approx 4.9\ mA \cdot cm^{-2};\ J_{IF} \approx 0\right)$, which accounts for the J_{sc} loss. At the maximum power point (~0.37 V), both channels contribute comparably $\left(J_{SRH} \approx 6.6\ mA \cdot cm^{-2};\ J_{IF} \approx 4\ mA \cdot cm^{-2}\right)$. The interface current increases exponentially with voltage, exceeds the bulk contribution above ~0.40 V and, at open circuit, accounts for ~31 of the ~39 mA cm^{-2} recombination current (~80 %). Bulk defects therefore limit carrier collection, whereas interface recombination limits V_{oc}. The selective reduction of each channel confirms this picture (Table S7). Halving the interface defect density increases V_{oc} by 68 mV and FF by 2.3 points, raising efficiency from 10.48 % to 12.57 %. Halving the band tail density mainly increases J_{sc} (+1.6 mA cm^{-2}), with a smaller V_{oc} gain (+13 mV), raising efficiency to 11.53 %. Interface passivation therefore yields the largest single efficiency gain, as it addresses the dominant recombination channel near V_{oc}.

In the bulk, reducing the band tail density is the most direct pathway towards recovering J_{sc} and FF, and it also contributes to V_{oc} [44]. This can be achieved through the structural-disorder control strategies discussed in Section 4.1. However, because the negative tail-state charge compensates for the double donor charge, a strong reduction of the band tail density must be accompanied by a reduction of the double donor density; otherwise, the double donor threshold returns towards $\approx 10^{15}\ cm^{-3}$ and the calibrated solar cell, with $N_{DD} = 1 \times 10^{16}\ cm^{-3}$, would undergo the collection collapse (Section 4.3).

Suppressing double donor-like defects is equally critical to preserving the junction electrostatics [15]. These donor-type states, commonly associated with Se-poor conditions and Sb_{Se}-related antisites, become particularly detrimental when their ionized charge, up to $2N_{DD}$, exceeds the background acceptor density. Above this threshold they invert the absorber to n-type and reverse the front field, causing a collapse of J_{sc} through interface recombination. The stoichiometry control strategies discussed in Section 4.1 target the formation of these compensating donors. This is consistent with high-efficiency Sb_2Se_3 fabrication strategies such as the thiourea and selenourea treatments reported by Zhao [9], which suppressed deep recombination-active defect states and improved device performance.

At the interface, improved passivation of the CdS/Sb_2Se_3 interface and replacement of CdS with wider-bandgap buffer layers would reduce interface recombination and parasitic absorption [33,49]. These strategies directly target the dominant V_{oc} loss and, according to the selective-reduction analysis, offer the largest single efficiency gain.

Finally, the comparison between the realistic defect-limited configuration ($\eta = 10.5\%$) and the configuration without bulk defects ($\eta = 15.4\%$) indicates that bulk defects alone do not fully determine the efficiency limit. Additional limitations related to interface recombination, band alignment, heterojunction energetics and depletion width also contribute to the remaining gap relative to the Shockley-Queisser limit [46] for the 1.1 eV bandgap used in the model. Further progress therefore requires a combined optimization of the heterojunction interface and the absorber bulk (structural disorder and donor-type compensation), with priority given to interface passivation [50].

4.5. Model limitations

The present results are obtained with an effective one-dimensional device model. SCAPS-1D solves the drift-diffusion and Poisson equations along the growth direction with scalar transport parameters, so the anisotropic transport of Sb_2Se_3, arising from its quasi-one-dimensional $[Sb_4Se_6]_n$ ribbon structure, is not explicitly represented [51]. The carrier mobilities used here should be understood as effective values along the growth direction, implicitly corresponding to the favorable ribbon orientation of the reference solar cell; the dependence of the solar cell performance on ribbon orientation cannot be assessed with this model. Grain boundaries are not spatially resolved, and their contribution to recombination and band bending is absorbed into the effective bulk defect and band tail parameters [52]. Similarly, the model assumes lateral homogeneity and therefore neglects thickness or compositional inhomogeneities, local shunt paths and lateral potential fluctuations. Bulk defects are distributed uniformly across the absorber thickness, so spatially correlated defects, such as defect clusters or defects segregated at grain boundaries or near the interface, are not considered. In addition, the microscopic assignments of the defects (V_{Se}, Sb_{Se}, V_{Sb}) are effective interpretations, the CdS/Sb_2Se_3 interface defects are represented by an interface defect density at a single energy level rather than by a continuous energy distribution of interface states, and the bandgap, carrier mobilities and Urbach energy are fixed input parameters. Consequently, the calibrated defect parameters are effective quantities that are not uniquely determined; the $\sigma \cdot N_t$ analysis (Fig. S2) identifies the calibrated set only as the best fit within the explored parameter space, and the conclusions should be interpreted as identifying the electrostatic and recombination mechanisms that govern device behavior within an effective 1D description, rather than as quantitative predictions for

Table 8
Tolerance thresholds of the bulk defects extracted from the single-defect sweeps. Thresholds are defined relative to the solar cell without bulk defects or, for the double donor sweep with band tails, to the solar cell with band tails only (Supporting Information Table S4 and Fig. S4).

Configuration	η-1 absolute point (cm^{-3})	J_{sc} – 10 % (cm^{-3})	Transition width (decades)	Limiting mechanism
DD only	4.0×10^{14}	1.1×10^{15}	0.36	Field reversal and interface recombination
BT only	6.5×10^{14}	1.3×10^{16}	1.7	Bulk SRH recombination
DD with BT	2.4×10^{16}	3.1×10^{16}	< 0.44	Compensation of the DD charge by tail states

specific microstructures. Two- or three-dimensional simulations that explicitly include grain boundaries and orientation-dependent transport would be required to address these effects.

5. Conclusions

SCAPS-1D model was developed and experimentally calibrated to investigate the device-level consequences of intrinsic defects and disorder in Sb_2Se_3 solar cells. Unlike conventional one-parameter sensitivity studies, the full-factorial defect analysis identified not only the individual effects of representative defect species but most importantly also their mutual interactions and resulting performance limitations.

The simulations revealed that considered defect populations in Sb_2Se_3 are not equally detrimental on solar cell performance within the investigated parameter space. Under the parameter set adopted for the reference solar cell, band tail states associated with structural disorder produce the largest reduction in quasi-Fermi level splitting and therefore contribute strongly to the simulated open-circuit voltage deficit. Near open circuit, however, recombination at CdS/Sb2Se3 interface accounts for 80 % of the recombination current, and halving the interface defect density yields the largest single efficiency gain (10.48 % to 12.57 %). Double donor-like defects primarily affect the electrostatic compensation of the native p-type absorber, leading to degradation of carrier extraction and fill factor. Under the adopted absorber doping, their impact becomes particularly pronounced at concentrations in the range of approximately 10^{15}–10^{16} cm^{-3}, where a threshold-like degradation of solar cell performance is observed. This concentration range is specific to the adopted device and defect parameters and should not be interpreted as a universal double donor concentration threshold for Sb_2Se_3. In contrast, single donor and acceptor defects produce comparatively minor impact within the investigated parameter space.

A central finding of the experimentally calibrated SCAPS-1D simulations is that the dominant defect families interact non-linearly. Band tail disorder and double donor defects influence different aspects of device operation, yet their coexistence generates a co-limited regime that closely reproduces the efficiency and voltage characteristics of current high-performance Sb_2Se_3 solar cells. Solar cell performance thus cannot be described and understood by considering independent defect contributions alone. The coupled sensitivity analysis enabled the construction of the two-dimensional defect-tolerance map that defines the operational window for high-efficiency Sb_2Se_3 photovoltaics. The results show that suppression of both structural disorder and donor-type compensation defects, together with passivation of the CdS/Sb_2Se_3 interface, is required to achieve substantial efficiency gains in Sb_2Se_3 solar cells. This finding provides a practical framework for absorber optimization through simultaneous control of microstructural quality and stoichiometry.

More broadly, the present work establishes a quantitative link between defect chemistry, junction electrostatics, recombination dynamics, and photovoltaic figures of merit. For the calibrated device, the analysis suggests that the efficiency limitation originates from coupled bulk and interface limitations rather than from a single dominant recombination pathway. Future progress toward higher efficiencies will therefore require integrated strategies combining defect suppression, interface passivation, and heterojunction optimization.

CRediT authorship contribution statement

J.M. Delgado-Sanchez: Writing – original draft, Validation, Software, Investigation, Formal analysis, Data curation, Conceptualization. **E. Artegiani:** Writing – review & editing, Validation, Methodology, Formal analysis, Conceptualization. **B. Rezek:** Writing – review & editing, Validation, Conceptualization. **A. Romeo:** Writing – review & editing, Validation, Supervision, Methodology, Investigation, Conceptualization.

Declaration of competing interest

The authors declare the following financial interests/personal relationships which may be considered as potential competing interests: Jose-Maria Delgado-Sanchez reports financial support was provided by University of Seville. If there are other authors, they declare that they have no known competing financial interests or personal relationships that could have appeared to influence the work reported in this paper.

Appendix A. Supplementary data

Supplementary data related to this article can be found online at https://doi.org/10.1016/j.solidstatesciences.2026.108540.

Data availability

Data will be made available on request.

References

[1] Y. Zhou, L. Wang, S. Chen, S. Qin, X. Liu, J. Chen, D.-J. Xue, M. Luo, Y. Cao, Y. Cheng, E.H. Sargent, J. Tang, Thin-film Sb_2Se_3 photovoltaics with oriented one-dimensional ribbons and benign grain boundaries, Nat. Photonics 9 (2015) 409–415.
[2] S. Ghosh, E.O. López, A. do N. Barbosa, N.R.C. Huaman, J.G. da Silva Filho, S. A. Raza, R. Santos, F.L. Freire Jr., A. Mello, Comprehensive structural and surface investigation of Sb_2Se_3 thin-films, Surf. Interfaces 44 (2024) 103693.
[3] C. Chen, K. Li, J. Tang, Ten years of Sb_2Se_3 thin film solar cells, Sol. RRL 6 (7) (2022) 2200094.
[4] M. Birkett, W.M. Linhart, J. Stoner, L.J. Phillips, K. Durose, J. Alaria, J.D. Major, R. Kudrawiec, T.D. Veal, Band gap temperature-dependence of close-space sublimation grown Sb_2Se_3 by photo-reflectance, APL Mater. 8 (6) (2018) 084901.
[5] C. Chen, W. Li, Y. Zhou, C. Chen, M. Luo, X. Liu, K. Zeng, B. Yang, C. Zhang, J. Han, J. Tang, Optical properties of amorphous and polycrystalline Sb_2Se_3 thin films prepared by thermal evaporation, Appl. Phys. Lett. 107 (4) (2015) 043905.
[6] Y. Zhou, M. Leng, Z. Xia, J. Zhong, H. Song, X. Liu, B. Yang, J. Zhang, J. Chen, K. Zhou, J. Han, Y. Cheng, J. Tang, Solution-processed antimony selenide heterojunction solar cells, Adv. Energy Mater. 4 (8) (2014) 1301846.
[7] X. Liu, C. Chen, W. Liang, J. Zhong, M. Luo, J. Chen, D.J. Xue, D. Li, Y. Zhou, J. Tang, Improving the performance of Sb_2Se_3 thin film solar cells over 4% by controlled addition of oxygen during film deposition, Prog. Photovoltaics Res. Appl. 23 (12) (2015) 1828–1836.
[8] C. Chen, K. Li, S. Chen, L. Wang, S. Lu, Y. Liu, D. Li, H. Song, J. Tang, Efficiency improvement of Sb_2Se_3 solar cells via grain boundary inversion, ACS Energy Lett. 3 (10) (2018) 2335–2341.
[9] Y. Zhao, S. Wang, C. Li, B. Che, X. Chen, H. Chen, R. Tang, X. Wang, G. Chen, T. Wang, J. Gong, T. Chen, X. Xiao, J. Li, Regulating deposition kinetics via a novel additive-assisted chemical bath deposition technology enables fabrication of 10.57% efficiency Sb_2Se_3 solar cells, Energy Environ. Sci. 15 (12) (2022) 5118–5128.
[10] C. Chen, D.C. Bobela, Y. Yang, S. Lu, K. Zeng, C. Ge, B. Yang, L. Gao, Y. Zhao, M. C. Beard, J. Tang, Characterization of basic physical properties of Sb_2Se_3 and its relevance for photovoltaics, Front. Optoelectron. 10 (2017) 18–30.
[11] G. Liang, M. Chen, M. Ishaq, X. Li, R. Tang, Z. Zheng, Z. Su, P. Fan, X. Zhang, S. Chen, Crystal growth promotion and defects healing enable minimum open-circuit voltage deficit in antimony selenide solar cells, Adv. Sci. 9 (9) (2022) 2105142.
[12] A. Mandal, Defect-tolerant recombination junction enabling enhanced V_{oc} in Sb_2Se_3 solar cells via high-work-function metal oxides: a simulation perspective, Sol. RRL 9 (23) (2025) e202500669.
[13] T.D.C. Hobson, L.J. Phillips, O.S. Hutter, K. Durose, J.D. Major, Defect properties of Sb_2Se_3 thin film solar cells and bulk crystals, Appl. Phys. Lett. 116 (26) (2020) 261101.
[14] A. Stoliaroff, A. Lecomte, O. Rubel, S. Jobic, X. Zhang, C. Latouche, X. Rocquefelte, Deciphering the role of key defects in Sb_2Se_3, a promising candidate for chalcogenide-based solar cells, ACS Appl. Energy Mater. 3 (3) (2020) 2496–2509.
[15] S. Dong, G. Li, J. Hong, R. Qi, S. Yang, P. Yang, L. Sun, F. Yue, Deep defects limiting the conversion efficiency of Sb_2Se_3 thin-film solar cells, Phys. Chem. Chem. Phys. 25 (2023) 4617–4623.
[16] M. Huang, P. Xu, D. Han, J. Tang, S. Chen, Complicated and unconventional defect properties of the quasi-one-dimensional photovoltaic semiconductor Sb_2Se_3, Applied Materials & Interfaces 11 (2019) 15564–15572.
[17] U. Wijesinghe, G. Longo, O.S. Hutter, Defect engineering in antimony selenide thin film solar cells, Energy Adv. 2 (2023) 12.
[18] X. Liu, X. Xiao, Y. Yang, D. Xue, D. Li, C. Chen, S. Lu, L. Gao, Y. He, M.C. Beard, G. Wang, S. Chen, J. Tang, Enhanced Sb_2Se_3 solar cell performance through theory-guided defect control, Prog. Photovoltaics Res. Appl. 25 (10) (2017) 861–870.
[19] C.N. Savory, D.O. Scanlon, The complex defect chemistry of antimony selenide, J. Mater. Chem. A 17 (2019) 10739–10744.

[20] M. Huang, Z. Cai, S. Wang, X.-G. Gong, S.-H. Wei, S. Chen, More Se vacancies in Sb_2Se_3 under Se-rich conditions: an abnormal behavior induced by defect-correlation in compensated compound semiconductors, Small 17 (36) (2021) 2102429.
[21] X. Wang, S.R. Kavanagh, D.O. Scanlon, A. Walsh, Upper efficiency limit of Sb_2Se_3 solar cells, Joule 8 (7) (2024) 2105–2122.
[22] K. Zeng, D.-J. Xue, J. Tang, Antimony selenide thin-film solar cells, Semicond. Sci. Technol. 31 (2016) 063001.
[23] H. Chen, Z.-Q. Li, B. Sun, X.-D. Feng, Towards high-efficiency planar heterojunction antimony sulfide solar cells, Opt. Mater. 121 (2021) 111556.
[24] M. Burgelman, P. Nollet, S. Degrave, Modeling polycrystalline semiconductor solar cells, Thin Solid Films 361 (2000) 527–532.
[25] F. Rahman, M. Chowdhury, L. Marasamy, M.K.A. Mohammed, D. Haque, S.R. Al Ahmed, A. Irfan, A.R. Chaudhry, S. Goumri-Said, Improving the efficiency of a CIGS solar cell to above 31% with Sb_2S_3 as a new BSF: a numerical simulation approach by SCAPS-1D, RSC Adv. 14 (2024) 1924–1938.
[26] S. Smairi, B. Hartiti, A. batan, A. Ziti, H.J.T. Nkuissi, C. Rachidy, H. Benali, S. Keles, P. Thevenin, M. Ertugrul, Physical properties of Cu_2ZnSnS_4 absorber layer deposited by spray pyrolysis: effect of the temperature associated with SCAPS 1D simulation, Phys. B Condens. Matter 691 (2024) 416314.
[27] K.J. Abbas, A. Bahrami, Investigating the potential of WO_3 and WS_2 as Cd-free buffer layers in Sb_2Se_3-based thin-film solar cells: a numerical study with SCAPS-1D software, Sol. Energy Mater. Sol. Cells 272 (2024) 112891.
[28] M. Burgelman, J. Verschraegen, S. Degrave, P. Nollet, Modeling thin-film PV devices, Prog. Photovoltaics Res. Appl. 12 (23) (2004) 143–153.
[29] J. Verschraegen, M. Burgelman, Numerical modeling of intra-band tunneling for heterojunction solar cells in SCAPS, Thin Solid Films 515 (15) (2007) 6276–6279.
[30] S.S. Bal, A. Basak, U.P. Singh, Numerical modeling and performance analysis of Sb-based tandem solar cell structure using SCAPS-1D, Opt. Mater. 127 (2022) 112282.
[31] Y. Xiao, H. Wang, H. Kuang, Numerical simulation and performance optimization of Sb_2Se_3 solar cell with a hole transport layer, Opt. Mater. 108 (2020) 110414.
[32] J. Li, L. Xiong, X. Hu, J. Liang, C. Chen, F. Ye, J. Li, Y. Liu, W. Shao, T. Wang, C. Tao, G. Fang, Manipulating the morphology of CdS/Sb_2Se_3 heterojunction using a Mg-doped tin oxide buffer layer for highly efficient solar cells, J. Energy Chem. 66 (2022) 374–381.
[33] M.T. Islam, A.K. Thakur, Two stage modelling of solar photovoltaic cells based on Sb_2Se_3 absorber with three distinct buffer combinations, Sol. Energy 202 (2020) 304–315.
[34] L.-Y. Lin, L.-Q. Jiang, Y. Qiu, B.-D. Fan, Analysis of Sb_2Se_3/CdS based photovoltaic cell: a numerical simulation approach, J. Phys. Chem. Solid. 122 (2018) 19–24.
[35] S. Barthwal, R. Gupta, A. Kumar, K. Ramesh, S. Pathak, S. Karak, Band offset engineering in antimony sulfide (Sb_2Se_3) solar cells, using SCAPS simulation: a route toward PCE $>$ 10%, Optik 282 (2023) 170868.
[36] N.K. Jayswal, S. Rijal, B. Subedi, I. Subedi, Z. Song, R.W. Collins, Y. Yan, N. J. Podraza, Optical properties of thin film Sb_2Se_3 and identification of its electronic losses in photovoltaic devices, Sol. Energy 228 (2021) 28–44.
[37] I. Caño, P. Vidal-Fuentes, L. Calvo-Barrio, X. Alcobé, J.M. Asensi, S. Giraldo, Y. Sánchez, Z. Jehl, M. Placidi, J. Puigdollers, V. Izquierdo-Roca, E. Saucedo, Does Sb_2Se_3 admit nonstoichiometric conditions? How modifying the overall Se content affects the structural, optical, and optoelectronic properties of Sb_2Se_3 thin films, Energy, Environmental, and Catalysis Applications 14 (9) (2022) 11222–11234.
[38] M.A.K.L. Dissanayake, K. Paramanathan, G.K.R. Senadeera, C.A. Thorawattage, K. Balashangar, P. Ravirajan, B.S. Dassanayake, Optical transmission and photoconductivity of chemical bath-deposited CdS thin films for optoelectronic applications, Thin Solid Films 791 (2024) 140225.
[39] X. Wang, S.R. Kavanagh, D.O. Scanlon, A. Walsh, Four-electron negative-U vacancy defects in antimony selenide, Phys. Rev. B 108 (2023) 134102.
[40] A. Rockett, "The Materials Science of Semiconductors", Springer, New York, 2008.
[41] N. Spalatu, R. Krautmann, A. Katerski, E. Karber, R. Josepson, J. Hiie, I.O. Acik, M. Krunks, Screening and optimization of processing temperature for Sb_2Se_3 thin film growth protocol: interrelation between grain structure, interface intermixing and solar cell performance, Sol. Energy Mater. Sol. Cells 225 (2021) 111045.
[42] M. Courel, T. Jiménez, A. Arce-Plaza, D. Seuret-Jiménez, J.P. Morán-Lázaro, F. J. Sánchez-Rodríguez, A theoretical study on Sb_2Se_3 solar cells: the path to overcome the efficiency barrier of 8%, Sol. Energy Mater. Sol. Cells 201 (2019) 110123.
[43] M.U. Salman, M. Mehak, U. Ali, G.M.U. Din, S.M. Ramay, M. Younis, S. Atiq, Direct correlation between open-circuit voltage and quasi-Fermi level splitting in perovskite solar cells: a computational step involving thickness, doping, lifetime, and temperature variations for green solutions, RSC Adv. 15 (2025) 15618–15629.
[44] C. Chen, J. Tang, Open-circuit voltage loss of antimony chalcogenide solar cells: status, origin, and possible solutions, ACS Energy Lett. 5 (7) (2020) 2294–2304.
[45] C.K.G. Kwok, H. Tangara, N. Masuko, R. Scheer, S. Ishizuka, M.M. Islam, T. Sakurai, Effects of quasi-Fermi level splitting and band tail states on open circuit voltage towards high-efficiency Cu(In,Ga)Se_2 solar cells, Sol. Energy Mater. Sol. Cell. 269 (2024) 112767.
[46] M. Kumar, S. Rani, X. Wang, V.N. Singh, Unlocking the full potential of solar cell materials: parameter sensitivity analysis and optimization using response surface modelling, Mater. Adv. 6 (1) (2025) 423–432.
[47] W. Shockley, H.J. Queisser, Detailed balance limit of efficiency of p-n junction solar cells, J. Appl. Phys. 32 (1961) 510–519.
[48] J. Tao, X. Hu, J. Xue, Y. Wang, G. Weng, S. Chen, Z. Zhu, J. Chu, Investigation of electronic transport mechanisms in Sb_2Se_3 thin-film solar cells, Sol. Energy Mater. Sol. Cells 197 (2019) 1–6.
[49] N. Torabi, J.M. Delgado-Sanchez, E. Artegiani, J. Kulicek, B. Rezek, P. Jakuza, M. Meneghini, A. Romeo, How the absorber thickness affects the electrical and structural properties of Sb_2Se_3 solar cells, Mater. Sci. Semicond. Process. 206 (2026) 110428.
[50] A. Mo, Y. Feng, B. Yang, W. Dang, X. Liang, W. Cao, Y. Guo, T. Chen, Z. Li, Controlling unintentional defects enables high-efficient antimony selenide solar cells, Adv. Funct. Mater. 34 (29) (2024) 2316292.
[51] A. Saidarsan, S. Guruprasad, A. Malik, P. Basumatary, D.S. Ghosh, A critical review of unrealistic results in SCAPS-1D simulations: causes, practical solutions and roadmap ahead, Sol. Energy Mater. Sol. Cells 279 (2025) 113230.
[52] A. Kowsar, S.C. Debnath, S. Ul-Islam, M.J. Hossain, M. Hossain, A.K. Chowdhury, G. Hashmi, S.F.U. Farhad, An overview of solar cell simulation tools, Solar Energy Advances 5 (2025) 100077.